University of Glasgow
DEPARTMENT OF
AEROSPACE
ENGINEERING



# Application of PMB2D to Axisymmetric Flows

B. J. Gribben, K. J. Badcock and B. E. Richards

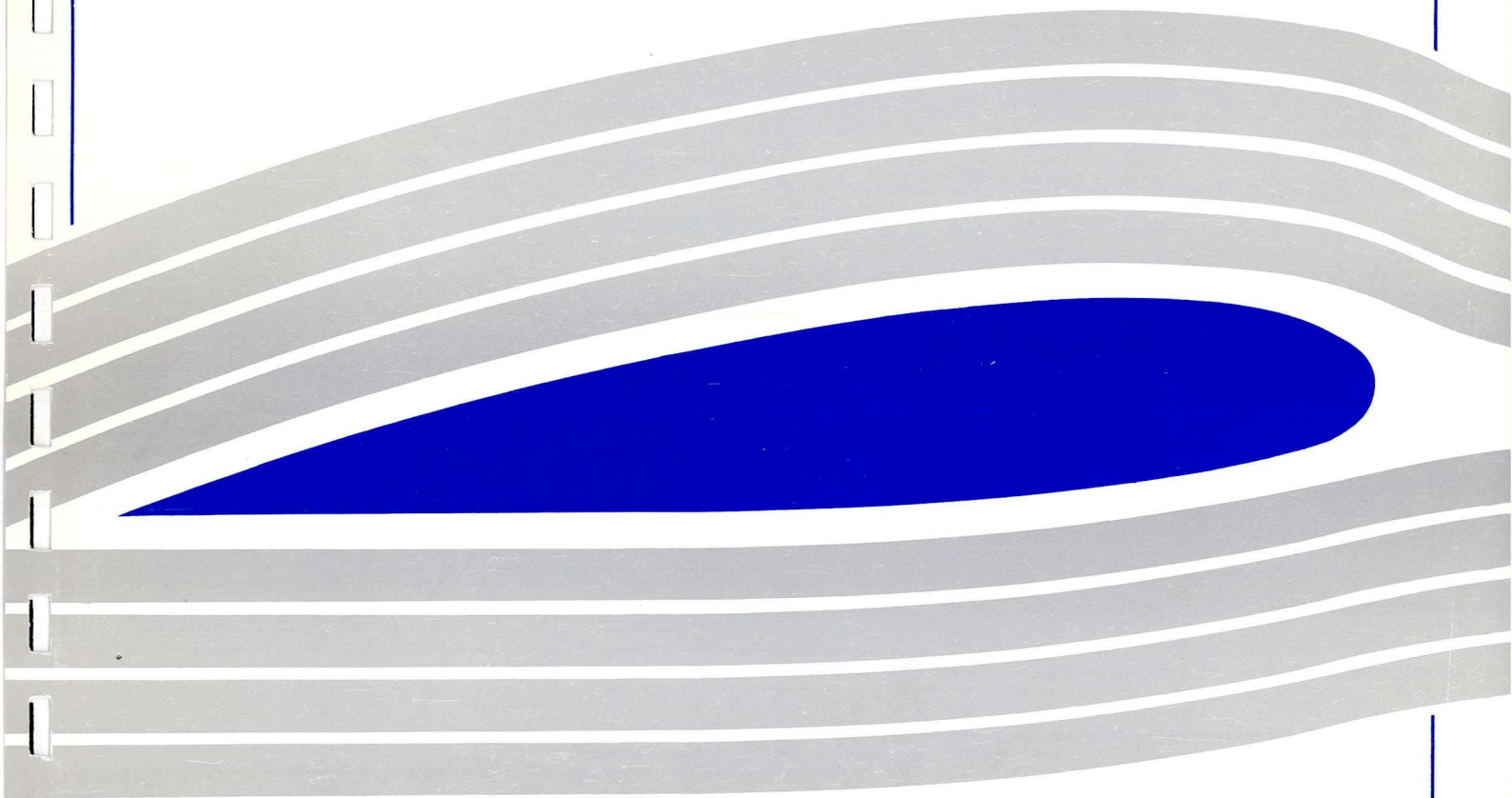

# Application of PMB2D to Axisymmetric Flows

B. J. Gribben, K. J. Badcock and B. E. Richards

University of Glasgow

Department of Aerospace Engineering

Report Number 9812

April 1998

# Abstract

This report describes how the two-dimensional planar flow solver PMB2D has been modified for axisymmetric flows. The equations describing axisymmetric flows are derived. The issue of conservation is discussed. The modified linear system arising at each implicit time step is detailed. Finally, results for inviscid, laminar and turbulent flow test cases are presented.

# Acknowledgements

Many thanks to all the CFD group for their assistance and guidance, especially my supervisors Dr. K.J. Badcock and Prof. B.E. Richards. The motivation for this work comes from Trevor Birch at DERA Bedford.

This work is supported by a University of Glasgow scholarship and sponsorship from DERA Bedford.

# Contents

**Abstract** ii

**Acknowledgements** iii

**Contents** iv

**List of Figures** vi

**1 Introduction** 1

1.1 Background . . . . . 1

1.2 Motivation . . . . . 2

1.3 Structure of report . . . . . 3

**2 The equations for axisymmetric flow** 4

2.1 Introduction . . . . . 4

2.2 Mass continuity . . . . . 4

2.3 Momentum conservation . . . . . 5

2.4 Energy equation . . . . . 7

2.5 Non-dimensional, Reynolds-averaged form . . . . . 9

2.6 The two-equation $k - \omega$ turbulence model . . . . . 11

2.7 Curvilinear form . . . . . 11

2.7.1 Mean flow equations . . . . . 11

2.7.2 Two equation $k - \omega$ turbulence model . . . . . 12

**3 Modified numerical scheme** **13**

3.1 Axisymmetric source terms . . . . . 13

3.2 Implicit scheme, mean flow equations . . . . . 15

3.3 Implicit scheme, $k - \omega$ equations . . . . . 17

**4 Application of axisymmetric PMB2D** **19**

4.1 Laminar Poiseuille flow . . . . . 19

4.1.1 Purpose of test case . . . . . 19

4.1.2 Description of test case . . . . . 19

4.1.3 Grid generation . . . . . 20

4.1.4 Boundary and initial conditions . . . . . 20

4.1.5 Results . . . . . 22

4.1.6 Conclusions . . . . . 22

4.2 ONERA B1 and B2 ogive cylinders . . . . . 25

4.2.1 Purpose of study . . . . . 25

4.2.2 Description of test cases . . . . . 25

4.2.3 Grid generation . . . . . 26

4.2.4 Boundary and initial conditions . . . . . 26

4.2.5 Results . . . . . 28

4.2.6 Numerical implementation of the turbulence model . . . . . 29

4.2.7 Conclusions . . . . . 30

4.3 GARTEUR Base Flow . . . . . 37

4.3.1 Purpose of study . . . . . 37

4.3.2 Description of test case . . . . . 37

4.3.3 Grid generation . . . . . 38

4.3.4 Boundary and initial conditions . . . . . 38

4.3.5 Results . . . . . 39

4.3.6 Conclusions . . . . . 41
4.4 Discussion . . . . . 48

**Appendices** **50**

**A The two-dimensional (planar) Navier-Stokes equations** **50**
A.1 Introduction . . . . . 50
A.2 Non-dimensional form . . . . . 50
A.3 Reynolds-averaged form . . . . . 52
A.4 Curvilinear form . . . . . 53

**B The two-equation $k-\omega$ turbulence model** **55**
B.1 Non-dimensional form . . . . . 55
B.2 Curvilinear form . . . . . 56

**Bibliography** **58**

# List of Figures


3.1 *Volume element in Cartesian coordinates* . . . . . 16

3.2 *Volume element in cylindrical coordinates* . . . . . 16

4.1 *Grid A used for Poiseuille flow test case* . . . . . 21

4.2 *Grid B used for Poiseuille flow test case* . . . . . 21

4.3 *Pressure Coefficient for Poiseuille flow test case* . . . . . 23

4.4 *Computed and Theoretical Velocity Profiles for Grid A, Poiseuille flow test case* . . . . . 23

4.5 *Computed and Theoretical Velocity Profiles for Grid B, Poiseuille flow test case* . . . . . 24

4.6 *Euler grid, ONERA B1 test case* . . . . . 27

4.7 *Nose region detail of Euler grid, ONERA B1 test case* . . . . . 27

4.8 *Convergence histories for B1 and B2 Euler calculations* . . . . . 31

4.9 *Convergence histories for B1 laminar Navier-Stokes calculation* . . . . 31

4.10 *Convergence history for B2 turbulent Navier-Stokes calculation (explicit CFL=0.4)* . . . . . 32

4.11 *Convergence history for B2 turbulent Navier-Stokes calculation(explicit CFL=0.6)* . . . . . 32

4.12 *Experimental and calculated pressure coefficient, ONERA B1* . . . . . 33

4.13 *Calculated skin friction coefficient, ONERA B1. (Comparison with ONERA results)* . . . . . 33

4.14 *Calculated local axial force coefficient, ONERA B1. (Comparison with ONERA results)* . . . . . 34
4.15 *Experimental and calculated pressure coefficient, ONERA B2* . . . . . 34
4.16 *Calculated skin friction coefficient, ONERA B2. (Comparison with ONERA results)* . . . . . 35
4.17 *Calculated local axial force coefficient, ONERA B2. (Comparison with ONERA results)* . . . . . 35
4.18 *Mach number contours for ONERA B2 test case* . . . . . 36
4.19 *Coarse grid used for GARTEUR afterbody 1B* . . . . . 39
4.20 *Symmetric line pressure coefficient, 1B* . . . . . 41
4.21 *Fine grid results, symmetric line pressure coefficient, 1B* . . . . . 42
4.22 *Laminar results, symmetric line pressure coefficient, 1B* . . . . . 42
4.23 *Pressure coefficient along base, 1B* . . . . . 43
4.24 *Axial velocity profile at x/D=0.1, 1B* . . . . . 43
4.25 *Axial velocity profile at x/D=0.5, 1B* . . . . . 44
4.26 *Axial velocity profile at x/D=1.5, 1B* . . . . . 44
4.27 *Turbulent kinetic energy profile at x/D=0.1, 1B* . . . . . 45
4.28 *Turbulent kinetic energy profile at x/D=0.5, 1B* . . . . . 45
4.29 *Turbulent kinetic energy profile at x/D=1.5, 1B* . . . . . 46
4.30 *Pressure contours, 1B* . . . . . 46
4.31 $\hat{\mathbf{P}}_k/\hat{\mathbf{D}}_k$ *contours, 1B* . . . . . 47
4.32 *Velocity vectors, 1B* . . . . . 47

# Chapter 1

# Introduction

## 1.1 Background

The planar two-dimensional, steady-state flow solver PMB2D developed by the CFD group has reached a level of maturity enabling application to a diverse range of aerodynamic problems. The main features of the flow solver are outlined here; for full details see [1], [2].

A cell-centred finite volume method is employed. Osher's scheme and MUSCL variable interpolation are used to discretise the convective terms and central differencing for the diffusive terms. The linear system arising at each implicit time step is solved using a Generalised Conjugate Gradient method. A Block Incomplete Lower-Upper (BILU) factorisation is used as a preconditioner. A structured multi-block grid system is employed. The BILU factorisation is decoupled between blocks to reduce communication. This results in efficient implementation on distributed memory parallel computers. An important feature of the flow solver is the use of approximate Jacobian matrices for the left hand side of the linear system. This has led to substantial reductions in memory and CPU-time requirements compared to the use of exact Jacobians. The $k-\omega$ turbulence model is employed with MUSCL variable interpolation and the Engquist-Osher scalar conservation law for the convective terms.

Methods for unsteady and incompressible flows are discussed in [3] and [4] respectively.

## 1.2 Motivation

In order to simulate large, complex aerodynamic problems using CFD a fully three-dimensional flow solver is necessary, using a multi-block approach or otherwise to cope with geometric complexity. However, there is a class of aerodynamic flows for which it is not necessary to resort to the complexity and expense of a full 3-D method. It is possible to make use of an existing two-dimensional flow solver to develop an axisymmetric flow solver, thus achieving a level of three-dimensional capability, albeit limited to axisymmetric geometries at zero incidence and sideslip. For this type of problem an axisymmetric rather than a full 3-D solver is a more efficient tool, considering the comparatively large amount of memory and CPU time required for 3-D calculations. The equations for axisymmetric flow can be cast in a form very similar to those for planar two-dimensional flow, which can then be solved using a numerical scheme with few alterations from the planar case. Examples of interest include slender bodies, base flows and nozzle/plume flows. This effort is therefore worthwhile because the modification required is relatively straightforward and the range of application surprisingly wide.

Several examples of computational aerodynamics codes solving the Euler and Navier-Stokes equations appear in the literature, for example for base flow applications [5], [6], [7], [8], [9], [10], [11] and missile forebodies [12], [13], [14], [15]. Some other applications are hypersonic flow [16] and internal nozzle flow [17]. Applications to underexpanded jets are discussed in [18]. Some flow solvers use the present approach

of considering the axisymmetric case as an extension of the two-dimensional case [5], [6], [9], [10], [11], [12], [14], [16], [17], thus allowing one flow solver to be used for two different types of flow. This work aims to investigate the modifications for axisymmetric flows to the method described above. This is worthwhile since the planar method has been observed to work well for high speed flows which are frequently encountered by axisymmetric bodies. Specifically, we shall consider supersonic flow around forebodies, underexpanded jet plumes and high speed base flows.

## 1.3 Structure of report

This report begins by presenting the equations for axisymmetric flow. Comparison is made with the equations for planar flow. The alterations made to the original linear system and the issue of maintaining a conservative numerical scheme are then discussed. The remainder of the report concerns the application of the axisymmetric flow solver to various test cases to evaluate accuracy and efficiency in solving a range of flows, and hence the utility of the flow solver to industry.

# Chapter 2

# The equations for axisymmetric flow

## 2.1 Introduction

In this chapter the Navier-Stokes equations and the two-equation $k-\omega$ turbulence model are presented in forms suitable for axisymmetric flow; the equations are written in cylindrical coordinates $(r, \theta, z)$ with the assumptions of zero angle of incidence and sideslip $(\partial/\partial\theta = 0)$ and no spin $(v_\theta = 0)$. A large part of their derivation from general vector/tensor forms is also included for completeness. This should help to highlight the origins and purpose of the 'extra' terms present in the axisymmetric equations compared to the two-dimensional equations.

## 2.2 Mass continuity

The equation of mass conservation, or continuity equation, is written in conservation form as [20],[21]:

$$\frac{\partial \rho}{\partial t} + \nabla.(\rho \mathbf{V}) = 0 \tag{2.1}$$

where $\rho$ is the fluid density and $\mathbf{V}$ is the velocity vector which has components $(v_r, v_\theta, v_z)$ in cylindrical coordinates. The divergence of a vector $\mathbf{A}$ in a cylindrical

frame is

$$\nabla.\mathbf{A} = \frac{\partial A_r}{\partial r} + \frac{A_r}{r} + \frac{1}{r}\frac{\partial A_\theta}{\partial \theta} + \frac{\partial A_z}{\partial z} \tag{2.2}$$

and therefore in a cylindrical frame equation (2.1) becomes

$$\frac{\partial \rho}{\partial t} + \frac{\partial}{\partial r}(\rho v_r) + \frac{1}{r}\frac{\partial}{\partial \theta}(\rho v_\theta) + \frac{\partial}{\partial z}(\rho v_z) = -\frac{\rho v_r}{r} \tag{2.3}$$

With our assumptions of axisymmetric flow with no spin this reduces to

$$\frac{\partial \rho}{\partial t} + \frac{\partial}{\partial r}(\rho v_r) + \frac{\partial}{\partial z}(\rho v_z) = -\frac{\rho v_r}{r} \tag{2.4}$$

## 2.3 Momentum conservation

The equations of motion or momentum equations neglecting body forces can be written in vector form as [20]

$$\rho\frac{\partial \mathbf{V}}{\partial t} + \rho\mathbf{V}.\nabla\mathbf{V} + \nabla p - \frac{\mu}{3}\nabla(\nabla.\mathbf{V}) - \mu\nabla^2\mathbf{V} = 0 \tag{2.5}$$

where $\mathbf{V}$ is the velocity vector. When expanding the vector terms in equation (2.5) it should be recalled that in cylindrical coordinates the unit vectors are not invariant in space [21],[22]. Following equation (2.2), the divergence of velocity in cylindrical coordinates is given by

$$\nabla.\mathbf{V} = \frac{\partial v_r}{\partial r} + \frac{v_r}{r} + \frac{1}{r}\frac{\partial v_\theta}{\partial \theta} + \frac{\partial v_z}{\partial z} \tag{2.6}$$

The strain tensor $\nabla\mathbf{V}$ in cylindrical coordinates is:

$$\nabla\mathbf{V} = \begin{pmatrix} \frac{\partial v_r}{\partial r} & \frac{\partial v_\theta}{\partial r} & \frac{\partial v_z}{\partial r} \\ \frac{1}{r}\frac{\partial v_r}{\partial \theta} - \frac{v_\theta}{r} & \frac{1}{r}\frac{\partial v_\theta}{\partial \theta} + \frac{v_r}{r} & \frac{1}{r}\frac{\partial v_z}{\partial \theta} \\ \frac{\partial v_r}{\partial z} & \frac{\partial v_\theta}{\partial z} & \frac{\partial v_z}{\partial z} \end{pmatrix} \tag{2.7}$$

Expanding the Laplacian of the velocity vector in cylindrical coordinates gives

$$\nabla^2\mathbf{V} \;=\; \nabla.(\nabla\mathbf{V}) \;=$$

$$\begin{pmatrix} \frac{\partial}{\partial r}\left(\frac{\partial v_r}{\partial r}\right)+\frac{1}{r}\frac{\partial v_r}{\partial r}+\frac{1}{r}\frac{\partial}{\partial\theta}\left(\frac{1}{r}\frac{\partial v_r}{\partial\theta}-\frac{v_\theta}{r}\right)+\frac{\partial}{\partial z}\left(\frac{\partial v_r}{\partial z}\right)-\frac{1}{r}\left(\frac{1}{r}\frac{\partial v_\theta}{\partial\theta}+\frac{v_r}{r}\right) \\ \frac{\partial}{\partial r}\left(\frac{\partial v_\theta}{\partial r}\right)+\frac{1}{r}\frac{\partial v_\theta}{\partial r}+\frac{1}{r}\frac{\partial}{\partial\theta}\left(\frac{1}{r}\frac{\partial v_\theta}{\partial\theta}+\frac{v_r}{r}\right)+\frac{\partial}{\partial z}\left(\frac{\partial v_\theta}{\partial z}\right)-\frac{1}{r}\left(\frac{1}{r}\frac{\partial v_r}{\partial\theta}-\frac{v_\theta}{r}\right) \\ \frac{\partial}{\partial r}\left(\frac{\partial v_z}{\partial r}\right)+\frac{1}{r}\frac{\partial v_z}{\partial r}+\frac{1}{r}\frac{\partial}{\partial\theta}\left(\frac{1}{r}\frac{\partial v_z}{\partial\theta}\right)+\frac{\partial}{\partial z}\left(\frac{\partial v_z}{\partial z}\right) \end{pmatrix} \tag{2.8}$$

Finally the pressure gradient term is

$$\nabla p \;=\; \begin{pmatrix} \frac{\partial p}{\partial r} \\ \frac{1}{r}\frac{\partial p}{\partial\theta} \\ \frac{\partial p}{\partial z} \end{pmatrix} \tag{2.9}$$

The equations (2.5) to (2.9) are the momentum conservation equations in cylindrical coordinates. It is convenient at this stage to introduce our assumptions concerning axisymmetry, viz. $\partial/\partial\theta = 0$ and $v_\theta = 0$ . The momentum equations in the radial ($r$) direction and axial ($z$) direction then become respectively

$$\rho\frac{\partial v_r}{\partial t}+\rho\left(v_r\frac{\partial v_r}{\partial r}+v_z\frac{\partial v_r}{\partial z}\right)+\frac{\partial p}{\partial r}-\frac{\mu}{3}\frac{\partial}{\partial r}\left(\frac{\partial v_r}{\partial r}+\frac{v_r}{r}+\frac{\partial v_z}{\partial z}\right) -\mu\left[\frac{\partial}{\partial r}\left(\frac{\partial v_r}{\partial r}\right)+\frac{1}{r}\frac{\partial v_r}{\partial r}+\frac{\partial}{\partial z}\left(\frac{\partial v_r}{\partial z}\right)-\frac{v_r}{r^2}\right] \;=\; 0 \tag{2.10}$$

$$\rho\frac{\partial v_z}{\partial t}+\rho\left(v_r\frac{\partial v_z}{\partial r}+v_z\frac{\partial v_z}{\partial z}\right)+\frac{\partial p}{\partial z}-\frac{\mu}{3}\frac{\partial}{\partial z}\left(\frac{\partial v_r}{\partial r}+\frac{v_r}{r}+\frac{\partial v_z}{\partial z}\right) -\mu\left[\frac{\partial}{\partial r}\left(\frac{\partial v_z}{\partial r}\right)+\frac{1}{r}\frac{\partial v_z}{\partial r}+\frac{\partial}{\partial z}\left(\frac{\partial v_z}{\partial z}\right)\right] \;=\; 0 \tag{2.11}$$

These equations can be simplified, using the continuity equation (2.4), to

$$\frac{\partial}{\partial t}(\rho v_r) + \frac{\partial}{\partial r}\left(\rho v_r^2 + p\right) - \frac{\partial \tau_{rr}}{\partial r} + \frac{\partial}{\partial z}(\rho v_r v_z) - \frac{\partial \tau_{rz}}{\partial z} = -\frac{\rho v_r^2}{r} + \frac{(\tau_{rr} - \tau_{\theta\theta})}{r} \quad (2.12)$$

$$\frac{\partial}{\partial t}(\rho v_z) + \frac{\partial}{\partial r}(\rho v_r v_z) - \frac{\partial \tau_{rz}}{\partial r} + \frac{\partial}{\partial z}\left(\rho v_z^2 + p\right) - \frac{\partial \tau_{zz}}{\partial z} = -\frac{\rho v_r v_z}{r} + \frac{\tau_{rz}}{r} \quad (2.13)$$

where the shear stress components are written as

$$\begin{aligned}
\tau_{rr} &= -\mu\left(2\frac{\partial v_r}{\partial r} - \frac{2}{3}\left(\frac{\partial v_r}{\partial r} + \frac{v_r}{r} + \frac{\partial v_z}{\partial z}\right)\right) \\
\tau_{zz} &= -\mu\left(2\frac{\partial v_z}{\partial z} - \frac{2}{3}\left(\frac{\partial v_r}{\partial r} + \frac{v_r}{r} + \frac{\partial v_z}{\partial z}\right)\right) \\
\tau_{\theta\theta} &= -\mu\left(2\frac{v_r}{r} - \frac{2}{3}\left(\frac{\partial v_r}{\partial r} + \frac{v_r}{r} + \frac{\partial v_z}{\partial z}\right)\right) \\
\tau_{rz} &= -\mu\left(\frac{\partial v_r}{\partial z} + \frac{\partial v_z}{\partial r}\right)
\end{aligned} \quad (2.14)$$

As will be seen later, it is convenient to re-arrange equations (2.12) and (2.13) to the following form (which resembles the planar equations)

$$\begin{aligned}
&\frac{\partial}{\partial t}(\rho v_r) + \frac{\partial}{\partial r}\left(\rho v_r^2 + p\right) - \frac{\partial}{\partial r}\left[\mu\left(2\frac{\partial v_r}{\partial r} - \frac{2}{3}\left(\frac{\partial v_z}{\partial z} + \frac{\partial v_r}{\partial r}\right)\right)\right] \\
&\quad + \frac{\partial}{\partial z}(\rho v_r v_z) - \frac{\partial}{\partial z}\left[\mu\left(\frac{\partial v_z}{\partial r} + \frac{\partial v_r}{\partial z}\right)\right] = -\frac{\rho v_r^2}{r} + \frac{4\mu}{3}\left(\frac{1}{r}\frac{\partial v_r}{\partial r} - \frac{v_r}{r^2}\right)
\end{aligned} \quad (2.15)$$

$$\begin{aligned}
&\frac{\partial}{\partial t}(\rho v_z) + \frac{\partial}{\partial r}(\rho v_r v_z) - \frac{\partial}{\partial r}\left[\mu\left(\frac{\partial v_z}{\partial r} + \frac{\partial v_r}{\partial z}\right)\right] + \frac{\partial}{\partial z}\left(\rho v_z^2 + p\right) \\
&\quad - \frac{\partial}{\partial z}\left[\mu\left(2\frac{\partial v_z}{\partial z} - \frac{2}{3}\left(\frac{\partial v_z}{\partial z} + \frac{\partial v_r}{\partial r}\right)\right)\right] = -\frac{\rho v_r v_z}{r} + \frac{\mu}{r}\left(\frac{1}{3}\frac{\partial v_r}{\partial z} + \frac{\partial v_z}{\partial r}\right)
\end{aligned} \quad (2.16)$$

## 2.4 Energy equation

The equation for the conservation of energy can be written as [21], [23]

$$\rho\frac{de}{dt} + p\left(\nabla.\mathbf{V}\right) = -\nabla.\mathbf{q} + \frac{\partial Q}{\partial t} + \Phi \quad (2.17)$$

where $e$ is the internal energy per unit mass, $\mathbf{q}$ is the heat transfer vector and $Q$ is the heat added per unit volume by external agencies. $\Phi$ is the dissipation function, which can be written as

$$\Phi = \mu\left[\left(\nabla\mathbf{V}+\nabla\mathbf{V}^T\right):\nabla\mathbf{V}-\frac{2}{3}\left(\nabla.\mathbf{V}\right)^2\right] \tag{2.18}$$

We are interested in the form of the energy conservation equation suitable for axisymmetric flow. In cylindrical coordinates, with the assumptions that $\partial/\partial\theta = 0$ and $v_\theta = 0$, the dissipation function becomes

$$\begin{aligned}\Phi = \mu\Bigg[&2\left(\frac{\partial u_r}{\partial r}\right)^2+2\left(\frac{u_r}{r}\right)^2+2\left(\frac{\partial u_z}{\partial z}\right)^2+\left(\frac{\partial u_z}{\partial r}+\frac{\partial u_r}{\partial z}\right)^2\\ &-\frac{2}{3}\left(\frac{\partial u_r}{\partial r}+\frac{u_r}{r}+\frac{\partial u_z}{\partial z}\right)^2\Bigg]\end{aligned} \tag{2.19}$$

Equation 2.17 can then be written, with the same assumptions, in the form

$$\begin{aligned}\rho\frac{de}{dt}+p\left(\frac{\partial v_r}{\partial r}+\frac{v_r}{r}+\frac{\partial v_z}{\partial z}\right) &= -\frac{\partial q_r}{\partial r}-\frac{q_r}{r}-\frac{\partial q_z}{\partial z}\\ &+\frac{\partial v_r}{\partial r}\tau_{rr}+\left(\frac{\partial v_r}{\partial z}+\frac{\partial v_z}{\partial r}\right)\tau_{rz}+\frac{\partial v_z}{\partial z}\tau_{zz}+\frac{v_r}{r}\tau_{\theta\theta}\end{aligned} \tag{2.20}$$

assuming also that there is also no external heat addition. It can be shown using the continuity equation (2.4) that

$$\frac{\partial}{\partial t}\left(\rho v_r\right)+\frac{\partial}{\partial r}\left(\rho v_r^2\right)+\frac{\partial}{\partial z}\left(\rho v_r v_z\right)+\frac{\rho v_r^2}{r} = \rho\frac{dv_r}{dt} \tag{2.21}$$

$$\frac{\partial}{\partial t}\left(\rho v_z\right)+\frac{\partial}{\partial r}\left(\rho v_r v_z\right)+\frac{\partial}{\partial z}\left(\rho v_z^2\right)+\frac{\rho v_r v_z}{r} = \rho\frac{dv_z}{dt} \tag{2.22}$$

The following equation is obtained by substituting equation (2.21) into (2.12) multiplied by $v_r$, and adding this to the equation obtained by substituting (2.22) into equation (2.13) multiplied by $v_z$ :

$$\begin{aligned}\rho\frac{d}{dt}\left(v_r^2/2+v_z^2/2\right)+v_r\frac{\partial p}{\partial r}+v_z\frac{\partial p}{\partial z}-v_r\frac{\partial\tau_{rr}}{\partial r}-v_r\frac{\partial\tau_{rz}}{\partial z}-v_z\frac{\partial\tau_{rz}}{\partial r}-v_z\frac{\partial\tau_{zz}}{\partial z}\\ = \frac{v_r\left(\tau_{rr}-\tau_{\theta\theta}\right)}{r}+\frac{v_z\tau_{rz}}{r}\end{aligned} \tag{2.23}$$

An equation representing the conservation of energy per unit mass is then obtained by adding together equations (2.20) and (2.23) :

$$\begin{aligned}\rho\frac{d}{dt}\left(e+v_r^2/2+v_z^2/2\right)+\frac{\partial}{\partial r}\left(pv_r+q_r\right)+\frac{pv_r}{r}+\frac{\partial}{\partial z}\left(pv_z+q_z\right)\\ -\frac{\partial}{\partial r}\left(v_r\tau_{rr}+v_z\tau_{rz}\right)-\frac{\partial}{\partial z}\left(v_z\tau_{zz}+v_r\tau_{rz}\right) &= \frac{v_r\tau_{rr}+v_z\tau_{rz}-q_r}{r}\end{aligned} \tag{2.24}$$

The total energy per unit volume $E_t$ is calculated as

$$E_t = \rho\left(e+\frac{1}{2}\left(v_r^2+v_z^2\right)\right)$$

It can be shown using the continuity equation (2.4) that

$$\rho\frac{d}{dt}\left(E_t/\rho\right) = \frac{\partial E_t}{\partial t}+\frac{\partial}{\partial r}\left(v_rE_t\right)+\frac{v_rE_t}{r}+\frac{\partial}{\partial z}\left(v_zE_t\right)$$

Hence equation (2.24) becomes

$$\begin{aligned}\frac{\partial E_t}{\partial t}+\frac{\partial}{\partial r}\left(v_r\left(E_t+p\right)\right)+\frac{\partial}{\partial z}\left(v_z\left(E_t+p\right)\right)-\frac{\partial}{\partial r}\left(v_r\tau_{rr}+v_z\tau_{rz}-q_r\right)\\ -\frac{\partial}{\partial z}\left(v_z\tau_{zz}+v_r\tau_{rz}-q_z\right) &= \frac{-v_r\left(E_t+p\right)+v_r\tau_{rr}+v_z\tau_{rz}-q_r}{r}\end{aligned} \tag{2.25}$$

As will be seen later, it is convenient here to express this equation in the following form (which resembles the planar equations):

$$\begin{aligned}&\frac{\partial E_t}{\partial t}+\frac{\partial}{\partial r}\left(v_r\left(E_t+p\right)\right)+\frac{\partial}{\partial z}\left(v_z\left(E_t+p\right)\right)\\ &\quad-\frac{\partial}{\partial r}\left\{v_r\left[\mu\left(2\frac{\partial u_r}{\partial r}-\frac{2}{3}\left(\frac{\partial u_r}{\partial r}+\frac{\partial u_z}{\partial z}\right)\right)\right]+v_z\left[\mu\left(\frac{\partial u_r}{\partial z}+\frac{\partial u_z}{\partial r}\right)\right]-q_r\right\}\\ &\quad-\frac{\partial}{\partial z}\left\{v_z\left[\mu\left(2\frac{\partial u_z}{\partial z}-\frac{2}{3}\left(\frac{\partial u_r}{\partial r}+\frac{\partial u_z}{\partial z}\right)\right)\right]+v_r\left[\mu\left(\frac{\partial u_r}{\partial z}+\frac{\partial u_z}{\partial r}\right)\right]-q_z\right\}\\ &\qquad=\frac{1}{r}\left[-v_r\left(E_t+p\right)+\mu\left(v_z\frac{\partial u_z}{\partial r}+\frac{v_z}{3}\frac{\partial u_r}{\partial z}-\frac{4v_r}{3}\frac{\partial u_z}{\partial z}\right)-q_r\right]\end{aligned} \tag{2.26}$$

## 2.5 Non-dimensional, Reynolds-averaged form

The equations shown above are in dimensional form. In practise it is more convenient to use non-dimensional quantities. The procedure used for non-dimensionalising is

described in sections A.2 and B.1. The Reynolds-averaging procedure, see appendix A.3, enables consideration of turbulent flow. The equations for mass continuity (2.4), momentum (2.16 and 2.15) and energy (2.26) become in non-dimensional, Reynolds-averaged form :

**Mass continuity**

$$\frac{\partial \rho}{\partial t} + \frac{\partial}{\partial r}(\rho v_r) + \frac{\partial}{\partial z}(\rho v_z) = -\frac{\rho v_r}{r} \tag{2.27}$$

**Momentum**

$$\begin{aligned}\frac{\partial}{\partial t}(\rho v_r) + \frac{\partial}{\partial r}(\rho v_r^2 + p) - \frac{\partial}{\partial r}\left[\frac{\mu+\mu_T}{Re}\left(2\frac{\partial v_r}{\partial r} - \frac{2}{3}\left(\frac{\partial v_z}{\partial z} + \frac{\partial v_r}{\partial r}\right) + \frac{2}{3}\rho k\right)\right] \\ + \frac{\partial}{\partial z}(\rho v_r v_z) - \frac{\partial}{\partial z}\left[\frac{\mu+\mu_T}{Re}\left(\frac{\partial v_z}{\partial r} + \frac{\partial v_r}{\partial z}\right)\right] = -\frac{\rho v_r^2}{r} + \frac{4(\mu+\mu_T)}{3Re}\left(\frac{1}{r}\frac{\partial v_r}{\partial r} - \frac{v_r}{r^2}\right)\end{aligned} \tag{2.28}$$

$$\begin{aligned}\frac{\partial}{\partial t}(\rho v_z) + \frac{\partial}{\partial r}(\rho v_r v_z) - \frac{\partial}{\partial r}\left[\frac{\mu+\mu_T}{Re}\left(\frac{\partial v_z}{\partial r} + \frac{\partial v_r}{\partial z}\right)\right] + \frac{\partial}{\partial z}(\rho v_z^2 + p) \\ - \frac{\partial}{\partial z}\left[\frac{\mu+\mu_T}{Re}\left(2\frac{\partial v_z}{\partial z} - \frac{2}{3}\left(\frac{\partial v_z}{\partial z} + \frac{\partial v_r}{\partial r}\right) + \frac{2}{3}\rho k\right)\right] = -\frac{\rho v_r v_z}{r} + \frac{\mu+\mu_T}{rRe}\left(\frac{1}{3}\frac{\partial v_r}{\partial z} + \frac{\partial v_z}{\partial r}\right)\end{aligned} \tag{2.29}$$

**Energy**

$$\begin{aligned}\frac{\partial E_t}{\partial t} + \frac{\partial}{\partial r}(v_r(E_t+p)) + \frac{\partial}{\partial z}(v_z(E_t+p)) \\ - \frac{\partial}{\partial r}\left\{v_r\left[\frac{\mu+\mu_T}{Re}\left(2\frac{\partial u_r}{\partial r} - \frac{2}{3}\left(\frac{\partial u_r}{\partial r} + \frac{\partial u_z}{\partial z}\right) + \frac{2}{3}\rho k\right)\right] + v_z\left[\frac{\mu+\mu_T}{Re}\left(\frac{\partial u_r}{\partial z} + \frac{\partial u_z}{\partial r}\right)\right]\right\} \\ - \frac{\partial}{\partial z}\left\{v_z\left[\frac{\mu+\mu_T}{Re}\left(2\frac{\partial u_z}{\partial z} - \frac{2}{3}\left(\frac{\partial u_r}{\partial r} + \frac{\partial u_z}{\partial z}\right) + \frac{2}{3}\rho k\right)\right] + v_r\left[\frac{\mu+\mu_T}{Re}\left(\frac{\partial u_r}{\partial z} + \frac{\partial u_z}{\partial r}\right)\right]\right\} \\ - \frac{\partial}{\partial r}\left\{\frac{1}{(\gamma-1)M_\infty^2}\left(\frac{\mu}{Pr} + \frac{\mu_T}{Pr_T}\right)\frac{\partial T}{\partial r}\right\} - \frac{\partial}{\partial z}\left\{\frac{1}{(\gamma-1)M_\infty^2}\left(\frac{\mu}{Pr} + \frac{\mu_T}{Pr_T}\right)\frac{\partial T}{\partial z}\right\} \\ = \frac{1}{r}\left[-v_r(E_t+p) + \frac{\mu+\mu_T}{Re}\left(v_z\frac{\partial u_z}{\partial r} + \frac{v_z}{3}\frac{\partial u_r}{\partial z} - \frac{4v_r}{3}\frac{\partial u_z}{\partial z} + \frac{2v_r}{3}\rho k\right)\right. \\ \left. + \frac{1}{(\gamma-1)M_\infty^2}\left(\frac{\mu}{Pr} + \frac{\mu_T}{Pr_T}\right)\frac{\partial T}{\partial r}\right]\end{aligned} \tag{2.30}$$

## 2.6 The two-equation $k-\omega$ turbulence model

The $k-\omega$ turbulence model of Wilcox [24] is written in non-dimensional, general vector-tensor form in appendix B.1. In cylindrical coordinates, for axisymmetric flow with no spin, this becomes

**Turbulence Kinetic Energy**

$$\begin{aligned}\frac{\partial}{\partial t}(\rho k)+\frac{\partial}{\partial r}(\rho k v_r)+\frac{\partial}{\partial z}(\rho k v_z)-\frac{1}{Re}\left\{\frac{\partial}{\partial r}\left[(\mu+\sigma^*\mu_T)\frac{\partial k}{\partial r}\right]+\frac{\partial}{\partial z}\left[(\mu+\sigma^*\mu_T)\frac{\partial k}{\partial z}\right]\right\}\\ =\ \mu_T P-\frac{2}{3}\rho k S-\beta^*\rho k\omega-\frac{\rho k v_r}{r}+\frac{1}{Re}\left\{\frac{1}{r}\left[(\mu+\sigma^*\mu_T)\frac{\partial k}{\partial r}\right]\right\}\end{aligned} \tag{2.31}$$

**Specific Dissipation Rate**

$$\begin{aligned}\frac{\partial}{\partial t}(\rho\omega)+\frac{\partial}{\partial r}(\rho\omega v_r)+\frac{\partial}{\partial z}(\rho\omega v_z)-\frac{1}{Re}\left\{\frac{\partial}{\partial r}\left[(\mu+\sigma\mu_T)\frac{\partial\omega}{\partial r}\right]+\frac{\partial}{\partial z}\left[(\mu+\sigma\mu_T)\frac{\partial\omega}{\partial z}\right]\right\}\\ =\ \alpha\frac{\omega}{k}\left[\mu_T P-\frac{2}{3}\rho k S\right]-\beta\rho\omega^2-\frac{\rho\omega v_r}{r}+\frac{1}{Re}\left\{\frac{1}{r}\left[(\mu+\sigma\mu_T)\frac{\partial\omega}{\partial r}\right]\right\}\end{aligned} \tag{2.32}$$

In the above relations,

$$\begin{aligned}P &= \left(\frac{\partial v_z}{\partial r}+\frac{\partial v_r}{\partial z}\right)^2+2\left[\left(\frac{\partial v_r}{\partial r}\right)^2+\left(\frac{\partial v_z}{\partial z}\right)^2+\left(\frac{v_r}{r}\right)^2\right]-\frac{2}{3}\left(\frac{\partial v_r}{\partial r}+\frac{\partial v_z}{\partial z}+\frac{v_r}{r}\right)^2\\ S &= \frac{\partial v_r}{\partial r}+\frac{\partial v_z}{\partial z}+\frac{v_r}{r}\end{aligned}$$

## 2.7 Curvilinear form

### 2.7.1 Mean flow equations

Compare the equations for axisymmetric flow, equations (2.27) to (2.30), with those for planar flow (see appendix A), swapping the radial ordinate $r$ for $y$ and the axial ordinate $z$ for $x$; the left hand sides of the equations are identical. Hence the axisymmetric equations can be considered as consisting of the 2-D equations plus a source-like correction term for axisymmetry. See section (3.1) for a discussion of the numerical implications. The transformation of the left-hand side of the equations into $(\xi,\eta)$ space is therefore identical to that described for the two-dimensional equations in appendix A.4. The right hand side of the transformed system of equations is written simply as

$$\frac{1}{J}\left(\hat{\mathbf{S}}^i+\hat{\mathbf{S}}^v\right) \tag{2.33}$$

after splitting the source-like term into inviscid and viscous parts.

### 2.7.2 Two equation $k-\omega$ turbulence model

The axisymmetric (equations 2.31 and 2.32) and the two-dimensional (see appendix B) formulations for the $k$ and $\omega$ equations can be compared in a similar manner to above; the axisymmetric equations can be considered as consisting of the 2-D equations plus a correction for axisymmetry. This correction is treated as an additional source term. Again the transformation of the left-hand side of the equations into $(\xi, \eta)$ space is the same as for the planar equations, see equation (B.5). The right hand side of the transformed system of equations can be written as

$$\frac{1}{J}\left(\hat{\mathbf{S}}_T + \hat{\mathbf{S}}_T^a\right) \tag{2.34}$$

where $\hat{\mathbf{S}}_T$ is the 'original' source term from the two-dimensional equations and $\hat{\mathbf{S}}_T^a$ contains the additional axisymmetric terms.

# Chapter 3

# Modified numerical scheme

## 3.1 Axisymmetric source terms

In the present method, the equations for axisymmetric flow are formulated to look like the planar flow equations except for a non-zero right-hand side which is treated as a source term (sections 2.7.1 and 2.7.2). The fluxes on the left-hand side are treated as in the planar case. In this way an existing planar flow solver can be modified easily for axisymmetric flow. This approach, which we will call here approach A, is popular in the literature, see [5], [6], [9], [10], [11], [12], [14], [16], [17]. Another approach appearing in the literature [14], [15], [19], approach B, uses an alternative formulation. The equations (3.1) show the axisymmetric Euler equations written in this manner. In this approach the source terms of approach A do not appear, being contained in the radial flux terms on the left-hand side. The source term here consists only of a pressure term in the radial momentum equation. The manner in which the fluxes are calculated for approach B cannot be taken directly from a planar method since the flux quantities are different.

$$\begin{aligned}
\frac{\partial}{\partial t}(r\rho) + \frac{\partial}{\partial r}(r\rho v_r) + \frac{\partial}{\partial z}(r\rho v_z) &= 0 \\
\frac{\partial}{\partial t}(r\rho v_r) + \frac{\partial}{\partial r}\left(r\left[\rho v_r^2 + p\right]\right) + \frac{\partial}{\partial z}(r\rho v_r v_z) &= p \\
\frac{\partial}{\partial t}(r\rho v_z) + \frac{\partial}{\partial r}(r\rho v_r v_z) + \frac{\partial}{\partial z}\left(r\left[\rho v_z^2 + p\right]\right) &= 0 \\
\frac{\partial}{\partial t}(r\rho E) + \frac{\partial}{\partial r}(r\rho v_r H) + \frac{\partial}{\partial z}(r\rho v_z H) &= 0
\end{aligned} \tag{3.1}$$

Good results are reported in the literature for both approaches and neither approach is reported to out-perform the other concerning accuracy or numerical implementation issues. Accepting then that both approaches are valid, it is nonetheless interesting here to briefly discuss and compare the approaches since such a discussion does not appear in the literature, and at the same time hopefully gain some insight

into the physical meaning of the source terms. For guidance we can refer to the application of the integral form of the conservation laws to a control volume fixed in space, which can form part of the derivation of the partial differential form of the equations [20]. This will shed some light on the origin and purpose of the source terms. Diagrams of control volumes for derivations in Cartesian $(x, y, z)$ and cylindrical $(r, \theta, z)$ space are shown in Figures 3.1 and 3.2.

Note that in Figure 3.2, the areas of the faces in the $(\theta, z)$ plane of the control volume are not equal; one has area $(r - dr/2)$ and the other $(r + dr/2)$. Note also that a pressure force acting normal to the control volume faces which are of area $drdz$ has a component in the radial direction. This means that when the integral forms of the conservation laws are evaluated for this control volume, involving fluxes through and normal stresses acting on each face, terms are retained in the resulting equations which cancel out due to symmetry in the equivalent procedure for the Cartesian control volume. These terms are the axisymmetric source terms. An example is shown below; first the equation for conservation of $x$-momentum is derived using the Cartesian control volume, then the radial momentum equation is derived using the cylindrical control volume and assuming $\partial/\partial\theta = 0$ and $v_\theta = 0$ . The equation for the conservation of momentum, discounting viscous effects and heat transfer, can be written in integral form as [20]

$$\frac{\partial}{\partial t}\int_\Omega \rho \mathbf{V} d\Omega \; + \; \oint_S \rho \mathbf{V} \left(\mathbf{V}.d\mathbf{S}\right) \; = \; -\oint_S p d\mathbf{S} \tag{3.2}$$

where $\Omega$ denotes the control volume and $S$ its surface.

**Momentum conservation in Cartesian coordinates ($x$-direction)**

Refer to equation (3.2) and Figure 3.1 :

$$\begin{aligned}
\frac{\partial(\rho u)}{\partial t}dxdydz - dydz\left[\rho u^2 - \frac{\partial(\rho u^2)}{\partial x}\frac{dx}{2} - \left(\rho u^2 - \frac{\partial(\rho u^2)}{\partial x}\frac{dx}{2}\right)\right] \\
- dxdz\left[\rho uv - \frac{\partial(\rho uv)}{\partial y}\frac{dy}{2} - \left(\rho uv - \frac{\partial(\rho uv)}{\partial y}\frac{dy}{2}\right)\right] \\
- dxdy\left[\rho uw - \frac{\partial(\rho uw)}{\partial z}\frac{dz}{2} - \left(\rho uw - \frac{\partial(\rho uw)}{\partial z}\frac{dz}{2}\right)\right] \\
= \; dydz\left[p - \frac{\partial p}{\partial x}\frac{dx}{2} - \left(p - \frac{\partial p}{\partial x}\frac{dx}{2}\right)\right]
\end{aligned}$$

which reduces to

$$\frac{\partial}{\partial t}(\rho u) + \frac{\partial}{\partial x}(\rho u^2 + p) + \frac{\partial}{\partial y}(\rho uv) + \frac{\partial}{\partial z}(\rho uw) \; = \; 0$$

**Momentum conservation in cylindrical coordinates with axisymmetry ($r$-direction)**

Refer to equation (3.2) and Figure 3.2 :

$$\begin{aligned}\frac{\partial(\rho v_r)}{\partial t} r d\theta dr dz - r d\theta dr \left[\rho v_r v_z - \frac{\partial(\rho v_r v_z)}{\partial z}\frac{dz}{2}\right] + r d\theta dr \left[\rho v_r v_z + \frac{\partial(\rho v_r v_z)}{\partial z}\frac{dz}{2}\right] \\ - \left(r - \frac{dr}{2}\right) d\theta dz \left[\rho v_r^2 - \frac{\partial(\rho v_r^2)}{\partial r}\frac{dr}{2}\right] + \left(r + \frac{dr}{2}\right) d\theta dz \left[\rho v_r^2 + \frac{\partial(\rho v_r^2)}{\partial r}\frac{dr}{2}\right] \\ = \left(r - \frac{dr}{2}\right) d\theta dz \left[p - \frac{\partial p}{\partial r}\frac{dr}{2}\right] - \left(r + \frac{dr}{2}\right) d\theta dz \left[p + \frac{\partial p}{\partial r}\frac{dr}{2}\right] \\ + p\frac{d\theta}{2} dr dx + p\frac{d\theta}{2} dr dx\end{aligned}$$

which reduces to

$$\frac{\partial}{\partial t}(\rho v_r) + \frac{\partial}{\partial r}(\rho v_r^2 + p) + \frac{\partial}{\partial z}(\rho v_r v_z) = -\frac{\rho v_r^2}{r}$$

The axisymmetric source terms can be interpreted physically as the additional mass, momentum or energy, compared to the planar case, which enters the control volume normal to the $(r, z)$ plane due to the axisymmetry of the flow. The effect of these terms is therefore equivalent to the effect of a surface source acting on the $(x, y)$ plane in the planar case. Restated, the axisymmetric equations written as in sections 2.7.1 and 2.7.2 can be considered as the planar two-dimensional equations with additional surface sources of mass, momentum and energy which account for the shape of the control volume in cylindrical coordinates. We can therefore conclude that the present treatment of our right-hand side as source terms, approach A, is reasonable. Approach B may be attractive to the researcher developing an axisymmetric flow solver 'from scratch' due to the neater appearance of the governing equations when written this way. The inclusion of the radial ordinate in the flux quantities, a feature which does not occur naturally from a direct application of the integral form of the conservation laws as shown above, does appear slightly artificial in that it is difficult to interpret physically.

## 3.2 Implicit scheme, mean flow equations

The integration in time of the discretised equations to a steady state is done using an implicit time-marching scheme. The linear system arising at each time step for the 2-D planar formulation can be summarised as [2] :

$$\left(\frac{I}{\Delta t} + \frac{\partial \mathbf{R}}{\partial \mathbf{W}}\right) \Delta \mathbf{W} = -\mathbf{R}^{(n)} \tag{3.3}$$

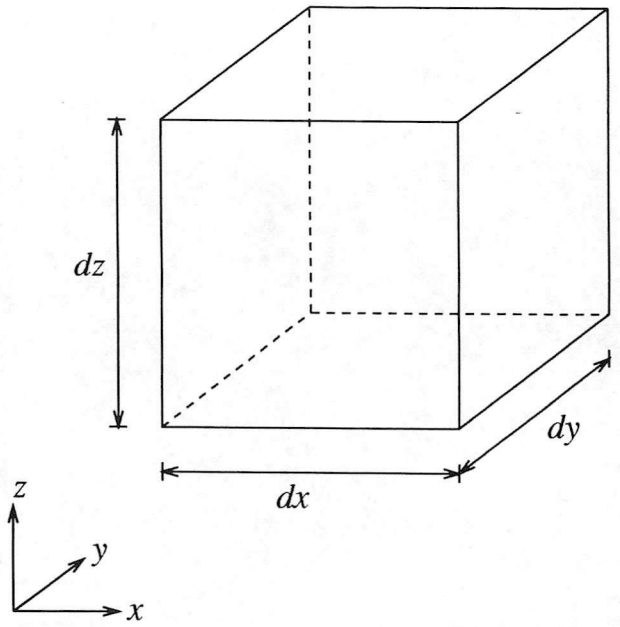


Figure 3.1: *Volume element in Cartesian coordinates*

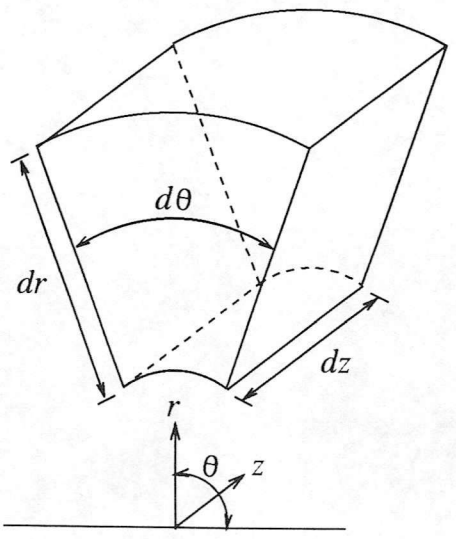


Figure 3.2: *Volume element in cylindrical coordinates*

where $\mathbf{W}$ is the vector of primitive variables, $\Delta\mathbf{W}$ is the update in $\mathbf{W}$ from time level $n$ to $n+1$, $\mathbf{R}^n$ is the flux residual arising from the spatial discretisation at the time level $n$, and $\Delta t$ is the time step. For the axisymmetric case, there are extra terms on the right-hand side, see equation(2.33). The axisymmetric inviscid part is treated implicitly, but the viscous part is treated explicitly. Numerical experiments have shown that it is necessary to have an implicit treatment for the axisymmetric inviscid terms if a tight restriction on the allowable time step is to be avoided. The explicit treatment of the axisymmetric viscous terms does not have a deleterious effect on stability or limit the allowable time step, on comparison with the original planar code, so an implicit treatment was not attempted. See Section 4.2.5 for an example of the importance of the implicit treatment for the axisymmetric inviscid terms. The modified linear system for the axisymmetric case is then written as :

$$\left(\frac{I}{\Delta t}+\frac{\partial\left(\mathbf{R}-\mathbf{H}^{i}\right)}{\partial\mathbf{W}}\right)\Delta\mathbf{W} \;=\; -\mathbf{R}^{(n)}+\mathbf{H}^{i(n)}+\mathbf{H}^{v(n)} \tag{3.4}$$

where $\mathbf{H}^i$ and $\mathbf{H}^v$ are the inviscid and viscous parts respectively of the discretised source term. System (3.4) is solved using an identical scheme [2] as used for (3.5). The inviscid source term Jacobian is evaluated as

$$\frac{\partial\mathbf{H}^{i}}{\partial\mathbf{W}} \;=\; -\frac{1}{r}\begin{bmatrix} v_r & 0 & \rho & 0 \\ v_r v_z & \rho v_r & \rho v_z & 0 \\ v_r^2 & 0 & 2\rho v_r & 0 \\ v_r\frac{|\vec{V}|^2}{2} & \rho v_r v_z & \frac{\gamma}{\gamma-1}p+\rho\frac{|\vec{V}|^2}{2}+\rho v_r^2 & \frac{\gamma}{\gamma-1}v_r \end{bmatrix} \tag{3.5}$$

where $|\vec{V}|^2 = v_r^2 + v_z^2$.

## 3.3 Implicit scheme, $k-\omega$ equations

The equations forming the turbulence model are solved in essentially the same manner as the mean flow equations. The linear system arising at each implicit time step for the 2-D planar formulation can be summarised as

$$\left(\frac{I}{\Delta t}+\frac{\partial\left(\mathbf{R}_T-\mathbf{H}_T\right)}{\partial\mathbf{W}_T}\right)\Delta\mathbf{W}_T \;=\; -\mathbf{R}_T^{(n)}+\mathbf{H}_T^{(n)} \tag{3.6}$$

where $\mathbf{W}_T = 1/J\,(k,\omega)^T$ is the vector of primitive variables, $\Delta\mathbf{W}_T$ is the update in $\mathbf{W}_T$ from time level $n$ to $n+1$ and $\mathbf{R}_T^{(n)}$ and $\mathbf{H}_T^{(n)}$ are the flux and source term residuals arising from the spatial discretisation respectively. For the axisymmetric case, there are extra terms on the right-hand side, see equation(2.34). The 'inviscid' parts of the additional source term are treated implicitly. The modified linear system for the axisymmetric case is then written as :

$$\left(\frac{I}{\Delta t} + \frac{\partial\left(\mathbf{R}_T - \mathbf{H}_T - \mathbf{H}_T^a\right)}{\partial \mathbf{W}_T}\right)\Delta\mathbf{W}_T \;=\; -\mathbf{R}_T^{(n)} + \mathbf{H}_T^{(n)} + \mathbf{H}_T^{a(n)} \tag{3.7}$$

where $\mathbf{H}_T^{a(n)}$ are the additional source term elements of the axisymmetric formulation. Its Jacobian is written as (discarding viscous terms)

$$\frac{\partial \mathbf{H}_T^a}{\partial \mathbf{W}} \;=\; -\frac{1}{r}\begin{bmatrix} \frac{5}{3}\rho v_r & 0 \\ 0 & \left(1+\frac{2}{3}\alpha\right)\rho v_r \end{bmatrix} \tag{3.8}$$

# Chapter 4

# Application of axisymmetric PMB2D

## 4.1 Laminar Poiseuille flow

### 4.1.1 Purpose of test case

An analytic solution of the Navier-Stokes equations exists for the case of laminar, incompressible, fully developed flow through a straight pipe of constant circular cross-section. A simulation of this type of flow using the laminar, axisymmetric version of PMB2D therefore provides a useful check on the formulation.

### 4.1.2 Description of test case

Fully developed flow in a pipe is characterised by a zero pressure gradient across the pipe, a constant pressure gradient along the pipe and a velocity profile which is invariant along the pipe. This situation arises because the pressure forces which drive the flow are exactly balanced by shear forces such that no acceleration can occur. For fully developed, steady, incompressible, laminar flow through a pipe of radius $r_o^*$ (axisymmetric Poiseuille flow) the analytic solution for the velocity components is written as [22] :

$$\begin{aligned} v_r^* &= 0 \\ v_z^* &= \frac{1}{4\mu^*}\frac{dp^*}{dz^*}\left(r^{*2} - r_o^{*2}\right) \end{aligned}$$

where $r$ and $z$ are the radial and axial directions respectively. The superscript $(^*)$ denotes dimensional quantities. The flow solver uses non-dimensional quantities, so it is more convenient to use this expression in the form

$$\begin{aligned} v_r &= 0 \\ v_z &= \frac{Re_l}{4\mu}\frac{dp}{dz}\left(r^2 - r_o^2\right) \end{aligned} \tag{4.1}$$

where

$$r = \frac{r^*}{l^*}, \qquad z = \frac{z^*}{l^*}, \qquad v_r = \frac{v_r^*}{V_\infty^*}, \qquad v_z = \frac{v_z^*}{V_\infty^*},$$

$$p = \frac{p^*}{\rho_\infty^* V_\infty^{*2}}, \qquad \mu = \frac{\mu^*}{\mu_\infty^*}, \qquad Re_l = \frac{\rho_\infty^* V_\infty^* l^*}{\mu_\infty^*}$$

and $l^*$ is a characteristic length, for example the overall length of the pipe. Here the reference conditions are taken as the conditions at the centre-line of the inlet. A subscript $\infty$ is retained here to denote such conditions in order to follow the convention used in section A.2 . The Mach number and Reynolds number of the flow considered correspond to low speed laminar flow: $M_\infty = 0.01$ and $Re_l = 500$ .

### 4.1.3 Grid generation

The grid generation for this test case is straightforward. Two single block grids were used. Details of the grid dimensions and spacings are summarised in table 4.1. The grids used are shown in figures 4.1 and 4.2. The flow is in the direction of increasing $z$. The grids are refined slightly towards the wall because of the higher viscous stresses expected in this area.

| *Name* | *Dimensions* | *Grid spacing at wall* |
|---|---|---|
| Grid A | 15 x 25 | 0.010 |
| Grid B | 31 x 51 | 0.005 |

Table 4.1: *Grids used for Poiseuille flow test case*

### 4.1.4 Boundary and initial conditions

At the outlet, the pressure is imposed at a value of $p = 1.0$ and the density and velocity components are extrapolated from the interior. At the inlet, the velocity is imposed using the analytic expression (4.1) normalised to unity at the centreline. The density is imposed at $\rho = 1.0$, the flow being incompressible, and the pressure is extrapolated from the interior. The walls are modelled as being adiabatic with no slip; the velocity components are set to zero and the pressure and density are

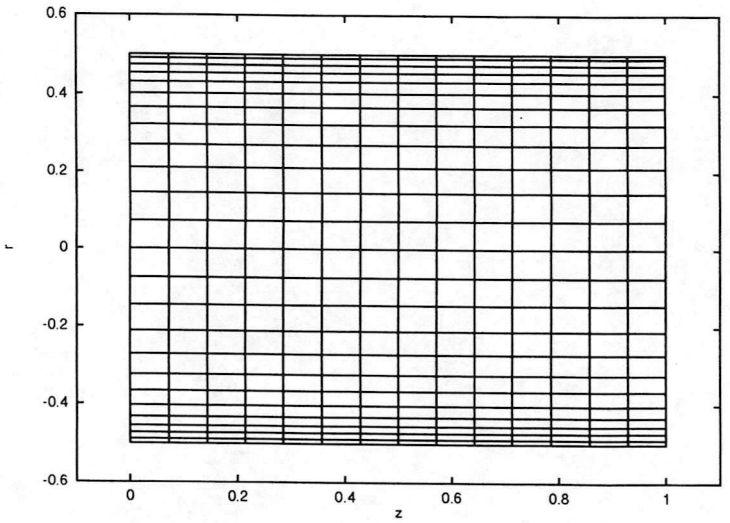


Figure 4.1: *Grid A used for Poiseuille flow test case*

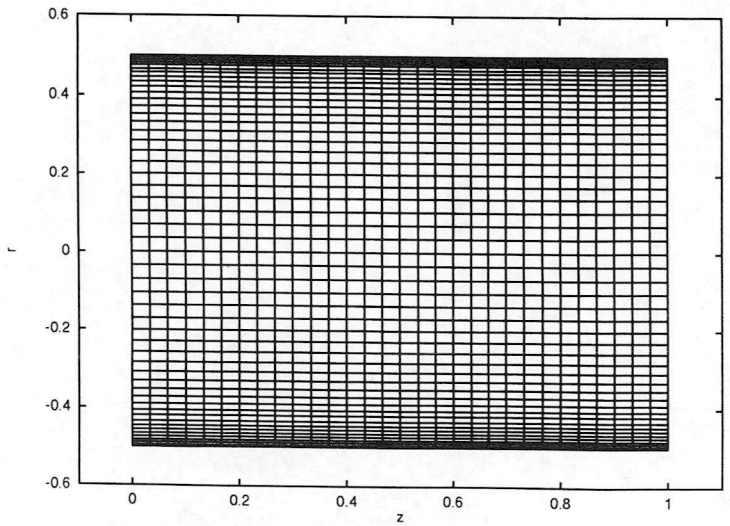


Figure 4.2: *Grid B used for Poiseuille flow test case*

extrapolated from the interior.

The following initial conditions were used throughout the domain: $\rho = 1.0$, $v_r = 0.0$, $v_z = 1.0$, $p = 1.0$.

### 4.1.5 Results

Solutions were obtained successfully using both grids. The convergence criterion used was the reduction by eight orders of magnitude of the L2 norm of the residual. The rate of convergence was slow in both cases, taking around 8000 work units in total[1]. This was expected when using a compressible flow solver for such a low speed flow, but is unimportant here where we are interested solely in the accuracy of the solution. The solutions obtained with the coarser grid A are identical to those obtained with grid B therefore the solutions can be considered grid converged. The pressure coefficient at every cell centre is plotted in figure 4.3 for the calculations on both grids. This clearly shows features which correspond with the analytic solution: there is a constant pressure gradient in the axial direction and no radial pressure variation. Figures 4.4 and 4.5 show the calculated velocity profile for grids A and B respectively. Both are compared with the exact solution for the calculated pressure gradient. There is excellent agreement between the theory and the calculation. The computed profiles shown were taken from central sections; any section could have been used because the profile does not change along the pipe.

Here we are concerned with axisymmetric flow. The analytic solution for planar Poiseuille flow [22] is similar but the maximum velocity is twice the magnitude of the axisymmetric case for the same axial pressure gradient. Planar Poiseuille flow has also been calculated using PMB2D, see [25]. The same approach was used as above and again very good agreement with theory was obtained. This underlines the important role played by the 'additional' viscous terms (section 2.7.1) in an axisymmetric formulation.

### 4.1.6 Conclusions

The laminar, axisymmetric version of PMB2D has been successfully applied to the case of Poiseuille flow through a pipe. Excellent agreement between theory and computational results has been obtained. The accuracy of the results establishes confidence in the axisymmetric viscous treatment.

[1] 1 work unit corresponds to the CPU time for 1 explicit time step

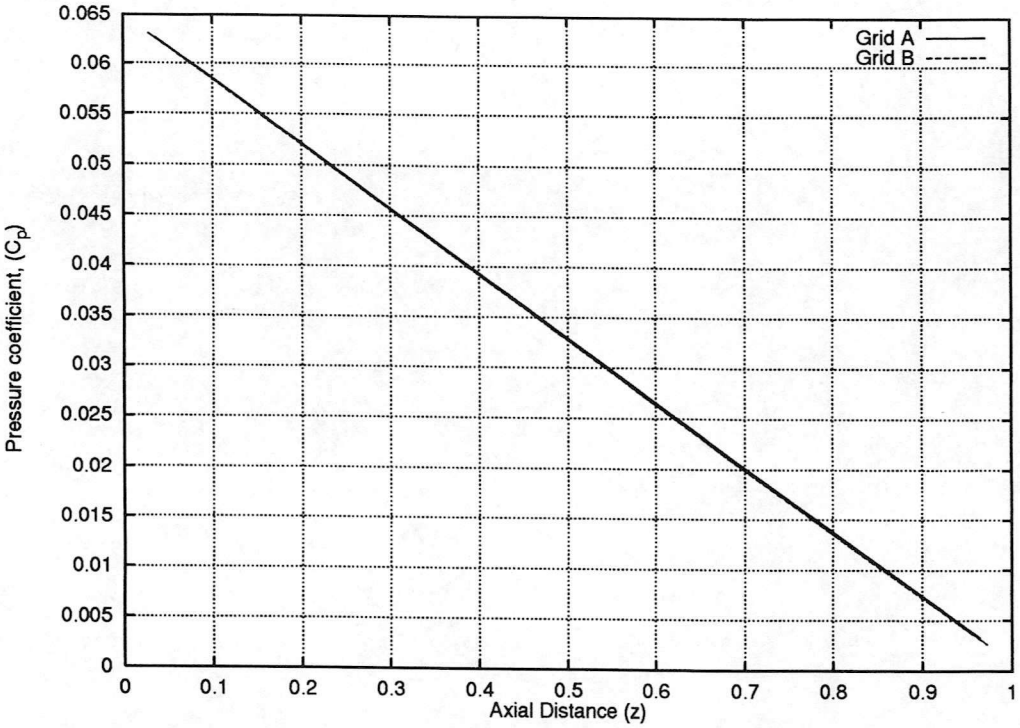


Figure 4.3: *Pressure Coefficient for Poiseuille flow test case*

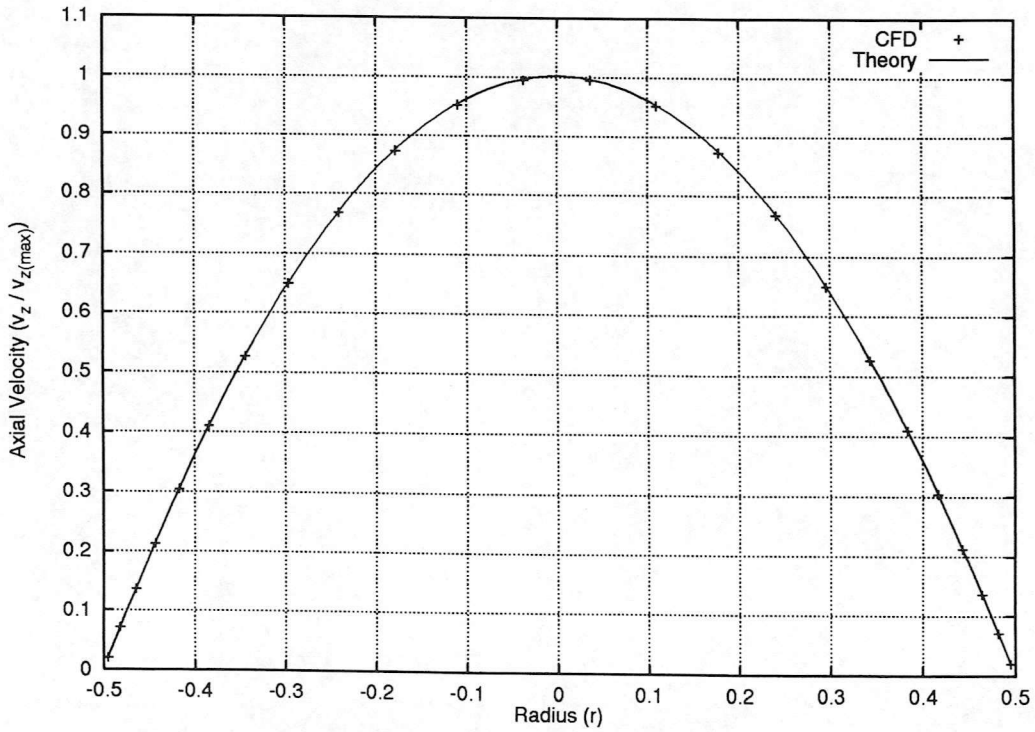


Figure 4.4: *Computed and Theoretical Velocity Profiles for Grid A, Poiseuille flow test case*

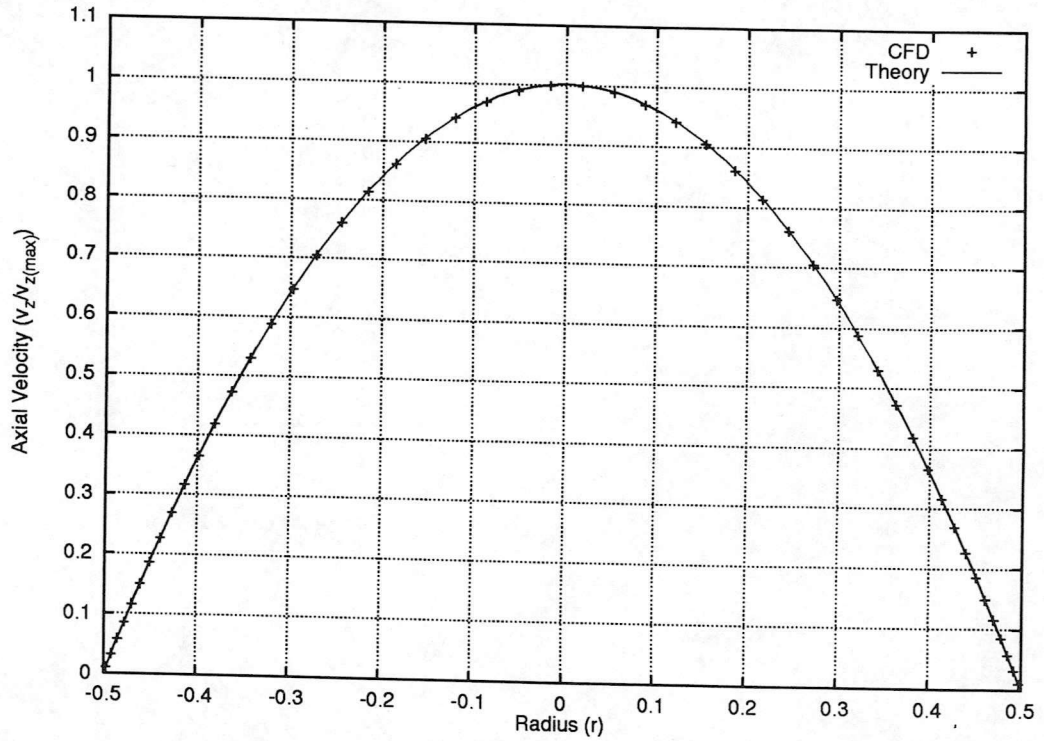


Figure 4.5: *Computed and Theoretical Velocity Profiles for Grid B, Poiseuille flow test case*

## 4.2 ONERA B1 and B2 ogive cylinders

### 4.2.1 Purpose of study

The ONERA B1 and B2 test case configurations appear frequently in the literature as benchmark test cases for slender-body supersonic flow, see for example [26]. Data from the original wind tunnel tests and from other computations are available for comparison. These are therefore useful test cases for code validation.

### 4.2.2 Description of test cases

#### ONERA B1

The ONERA B1 configuration consists of a pointed convex forebody continued tangentially by a circular cylinder of diameter D. The forebody is of length 3D and is described by the arc of a circle of radius 9.25D. The test conditions reported from the original experiment are as follows:

$$
\begin{aligned}
&\text{Laminar flow} \\
\text{Freestream Mach number, } M_\infty &= 2.0 \\
\text{Reynolds number, } Re_D &= 0.16 * 10^6 \\
\text{Freestream stagnation pressure, } p_{t\infty} &= 50 * 10^3 Pa \\
\text{Freestream stagnation temperature, } T_{t\infty} &= 330K \\
\text{Wall temperature, } T_w &\simeq 315K \; (adiabatic) \\
\text{Incidence, } \alpha &= 0^o
\end{aligned}
$$

#### ONERA B2

The ONERA B2 geometry is very similar to that of the B1. The convex forebody is described by a parabolic profile, equation (4.2) rather than a circular arc. Again the forebody is of length 3D. The test conditions reported from the original experiment are as follows:

$$
\begin{aligned}
\text{Turbulent flow} & \\
\text{Fixed transition at } z/D &= 0.15 \\
\text{Freestream Mach number, } M_\infty &= 2.0 \\
\text{Reynolds number, } Re_D &= 1.2 * 10^6 \\
\text{Freestream stagnation pressure, } p_{t\infty} &= 120 * 10^3 Pa \\
\text{Freestream stagnation temperature, } T_{t\infty} &= 300K \\
\text{Wall temperature, } T_w &\simeq 285K \; (adiabatic) \\
\text{Incidence, } \alpha &= 0^o
\end{aligned}
$$

$$\frac{r}{D} = \frac{1}{3}\left(\frac{z}{D}\right) - \frac{1}{18}\left(\frac{z}{D}\right)^2 \tag{4.2}$$

### 4.2.3 Grid generation

The grids used in this study were standard grids supplied by ONERA as part of a GARTEUR workshop. Two grids were supplied for each case, the coarser intended for inviscid (Euler) calculations and the finer for viscous calculations. Details of the grids are summarised in table 4.2. Grid B1c, the coarser grid for the B1 case, is shown in Figures 4.6 and 4.7. The other grids are very similar. All of the grids include a small nose boom, one cell in width, of very small but finite radius (1.0x10$^{-7}$D). This feature was intended to aid contributors to the workshop using three-dimensional flow solvers which would not handle the singularity at the nose. It was not needed here, but was retained since experiments using a modified grid with the nose boom removed showed that it has no effect on the solution.

| *Name* | *Dimensions* | *Grid spacing on cylinder surface* |
|---|---|---|
| B1c | 61 x 53 | $1.74 * 10^{-2}$ D |
| B1f | 61 x 85 | $2.00 * 10^{-4}$ D |
| B2c | 61 x 53 | $1.74 * 10^{-2}$ D |
| B2f | 61 x 85 | $2.50 * 10^{-5}$ D |

Table 4.2: *Grids used for ONERA B1 and B2 test cases*

### 4.2.4 Boundary and initial conditions

All variables were extrapolated from the interior across the outflow boundary. The wall boundary was modelled as being adiabatic with no slip. A characteristic-based far-field boundary condition was employed at the remaining two domain boundaries.

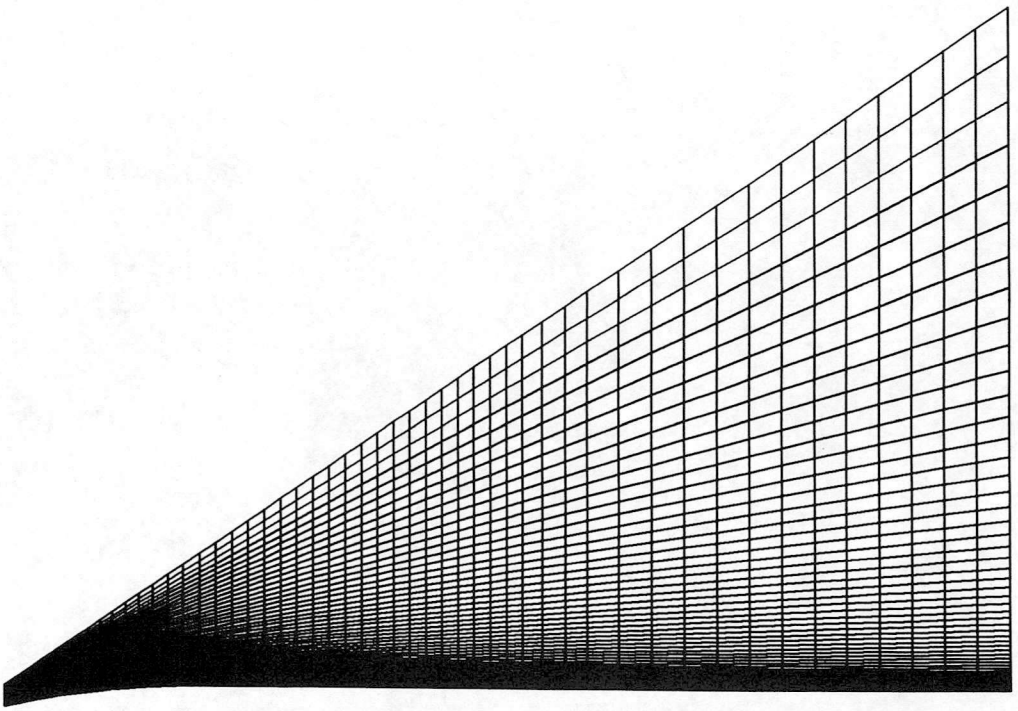

Figure 4.6: *Euler grid, ONERA B1 test case*

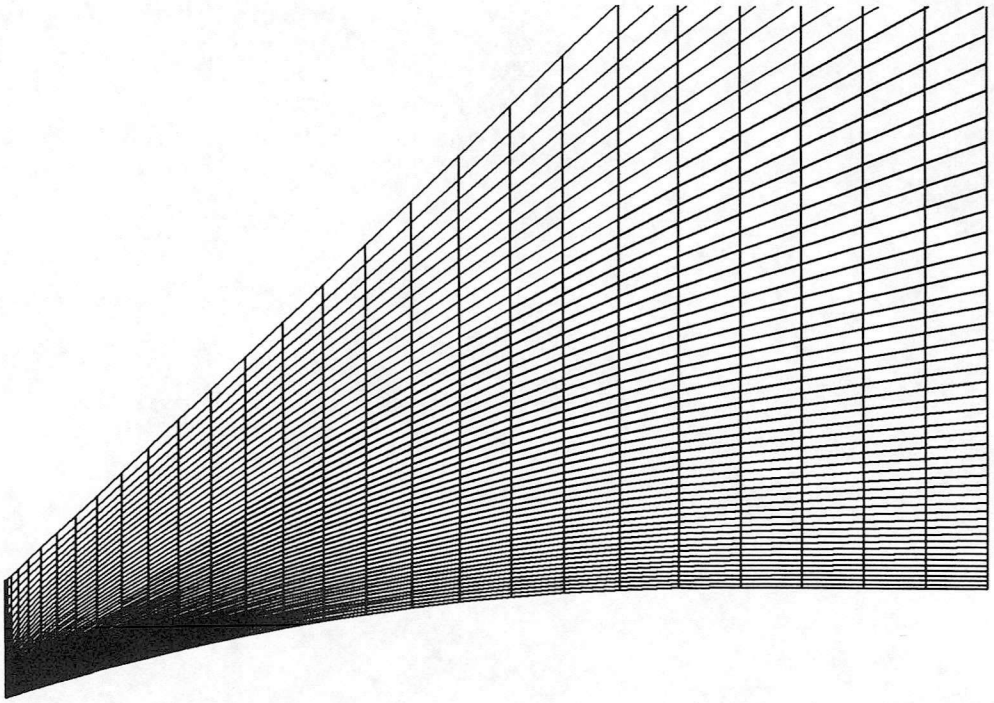

Figure 4.7: *Nose region detail of Euler grid, ONERA B1 test case*

### 4.2.5 Results

Solutions were obtained for all four cases: inviscid (Euler) calculations for B1 and B2, laminar Navier-Stokes for B1 and Reynolds-averaged Navier-Stokes with $k-\omega$ turbulence model for B2. A summary of the calculations performed is shown in table 4.3. Included in this table are the CPU times for each calculation on a Silicon Graphics Indy R5000. In each case, the calculation was considered converged when the L2 norm of the residual had reduced by eight orders of magnitude. Convergence histories for each case are shown in Figures 4.8 to 4.11. The B1 Euler calculation was also attempted using an explicit treatment for the axisymmetric inviscid terms to examine the effect of the implicit treatment, see Section 3.2. In order to obtain a solution it was necessary to use twice as many explicit steps before switching to the implicit scheme, and the implicit CFL number was limited to 50, rather than a value of 250 used in the calculation shown. As a result the overall time taken for the calculation was increased by 50%. This supports the present method where the implicit treatment is used.

| *Calculation* | *Grid used* | *CPU time* |
|---|---|---|
| B1, Euler | B1c | 50 s |
| B2, Euler | B2c | 47 s |
| B1, Laminar | B1f | 288 s |
| B2, Turbulent | B2f | 822 s |

Table 4.3: *Summary of calculations for ONERA B1 and B2*

Figures 4.12 to 4.17 show the calculated values of pressure coefficient, skin friction coefficient and local axial force. Comparison is made with experimental data [27] where possible and otherwise with other computations [28]. Table 4.4 shows a summary of the calculated total axial force coefficients: $Ca_p$ denotes the pressure component, $Ca_f$ the viscous component and $Ca$ is the total.

| *Calculation* | $Ca_p$ | $Ca_f$ | $Ca$ |
|---|---|---|---|
| B1, Euler | 0.0953 | - | 0.0953 |
| B2, Euler | 0.0947 | - | 0.0947 |
| B1, Laminar | 0.0985 | 0.0511 | 0.1496 |
| B2, Turbulent | 0.0982 | 0.1310 | 0.2292 |

Table 4.4: *Summary of calculated axial force coefficients*

Good agreement was obtained with the experimental values of pressure coefficient for the B1 case, see Figure 4.12. The calculated skin friction coefficient curve, see Figure 4.13, agrees well with the ONERA computational results over the forebody. However, the two curves begin to diverge downstream, and at $z/D = 15$ the ONERA

computation predicts nearly twice as much skin friction. The calculated local contribution to the axial force for the B1 case, Figure 4.14, shows up the same differences between the results i.e. a good match for the pressure component and a poor match for the viscous component. The axial force coefficient values quoted in Table 4.4 are calculated as the area underneath the local axial force curves. The good agreement of the pressure values with experiment shown (and with ONERA pressure results not shown) is encouraging from the point of view of verification of the flow solver. It is not possible at present to say much about the skin friction results since we only have the results from two computations, although the difference in results is disappointing. More computational results will be made available form the GARTEUR Action Group in the future.

The calculated pressure coefficient for the B2 case matches the experimental values very well over the forebody, but over the remainder of the surface the computational results seem to be offset slightly, see Figure 4.15. Comparison with the ONERA results for Cp values is not shown, but the agreement is very good. The calculated skin friction coefficient curves for the present calculation and from ONERA are in fairly good agreement, see Figure 4.16. Note that the $k - \omega$ turbulence model was used for the present calculation, and ONERA used a Baldwin-Lomax turbulence model. Comparing the local contribution to the axial force for the B2 case with the B1 case, Figures 4.14 and 4.17, for the B2 case the effect of viscous drag appears to be relatively more important. This is a trend that we expect since the B2 case is turbulent with a higher Reynolds number. Again it will be possible to read more into these results when other computational results become available.

### 4.2.6 Numerical implementation of the turbulence model

In the present method, a number of explicit (backwards Euler) iterations are performed before switching to the implicit scheme with a high, constant CFL number (say 250). Experience has shown that this is an effective way of initiating the calculation. During this explicit stage in the turbulent B2 calculation the scheme became unstable. This seemed to be caused by the appearance of small and negative values of $k$ and $\omega$. Other workers have also experienced such difficulties in the initial stages of a calculation when using two- and one-equation turbulence models [6], [29], [30], [31]. The various remedies reported apply specifically to implicit schemes. Here the problem arises during the explicit stage, and the straightforward remedy of limiting the values of $k$ and $\omega$ to be no less than the freestream values was applied. These limits were only used during the explicit stage. Figure 4.10 shows a convergence plot of the calculation. It is noted that the number of explicit iterations required is relatively large and that the residual for the turbulent quantities is small in the initial stages. An explicit CFL number of 0.4 was used here for both the mean flow and the turbulence equations. In an attempt to speed up the calculation by making the turbulent quantities do more work, the calculation was re-run using an explicit

CFL number of 0.4 for the mean flow equations and 0.6 for the turbulence equations. Figure 4.11 shows a convergence plot of the calculation. In this case less explicit steps were required and the overall CPU time for the calculation was reduced by nearly 20%.

When using an implicit scheme and a two- or one-equation turbulence model, the treatment of the source term Jacobian arising from the time linearisation of the updates for the turbulent quantities is reported to be important for stability, particularly during the initial stages of the calculation [6], [24], [29], [30], [31]. As discussed above, in our case the initial instability problem is dealt with during the explicit stage. The effect of the suggested modified implicit schemes was investigated in any case for the B2 problem. The modified schemes all involve some variation of the turbulent source term Jacobian in the form of neglecting off-diagonal terms, varying the size of coefficients or altering the terms in the matrix according to sign changes. The modified schemes showed no improvement, either regarding robustness (the number of explicit steps required was unchanged) or speed of convergence.

### 4.2.7 Conclusions

The axisymmetric version of PMB2D has been successfully applied to two supersonic slender-body aerodynamics problems. The results have been compared with experimental data and computational data from other sources. At present the agreement with other data is encouraging although a fuller analysis will be possible in the future when further data becomes available. Together with other succesful applications of the code to this type of flow [32], this gives confidence in the accuracy of the code for this type of problem. Some useful insights into the numerical implementation of the $k - \omega$ turbulence model have also been gained.

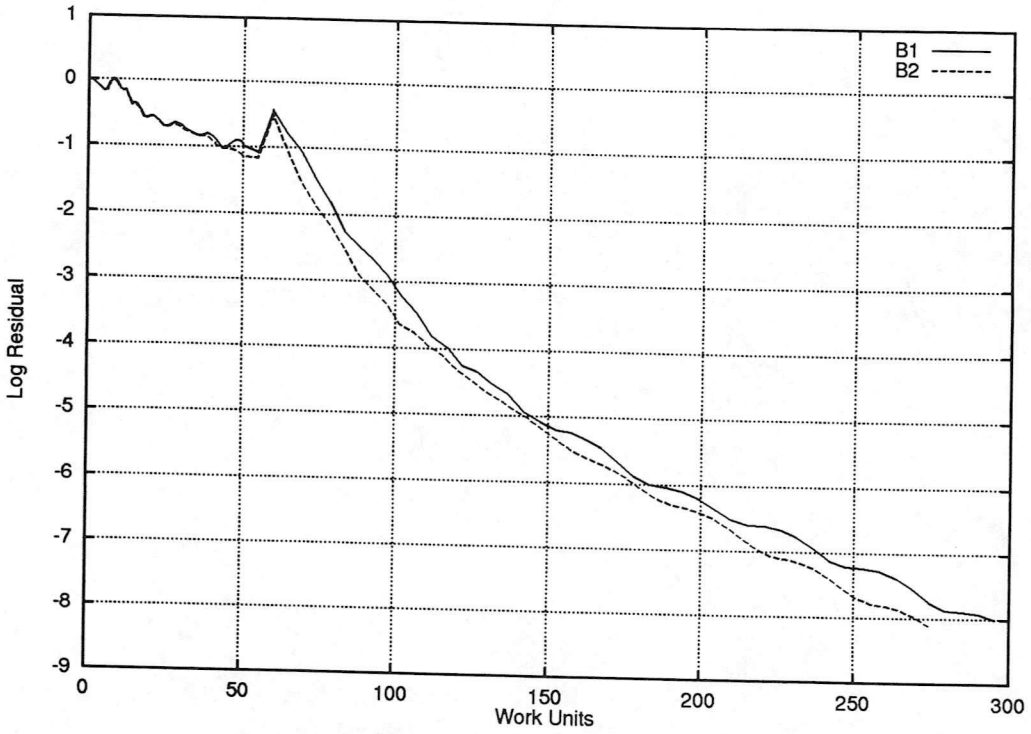


Figure 4.8: *Convergence histories for B1 and B2 Euler calculations*

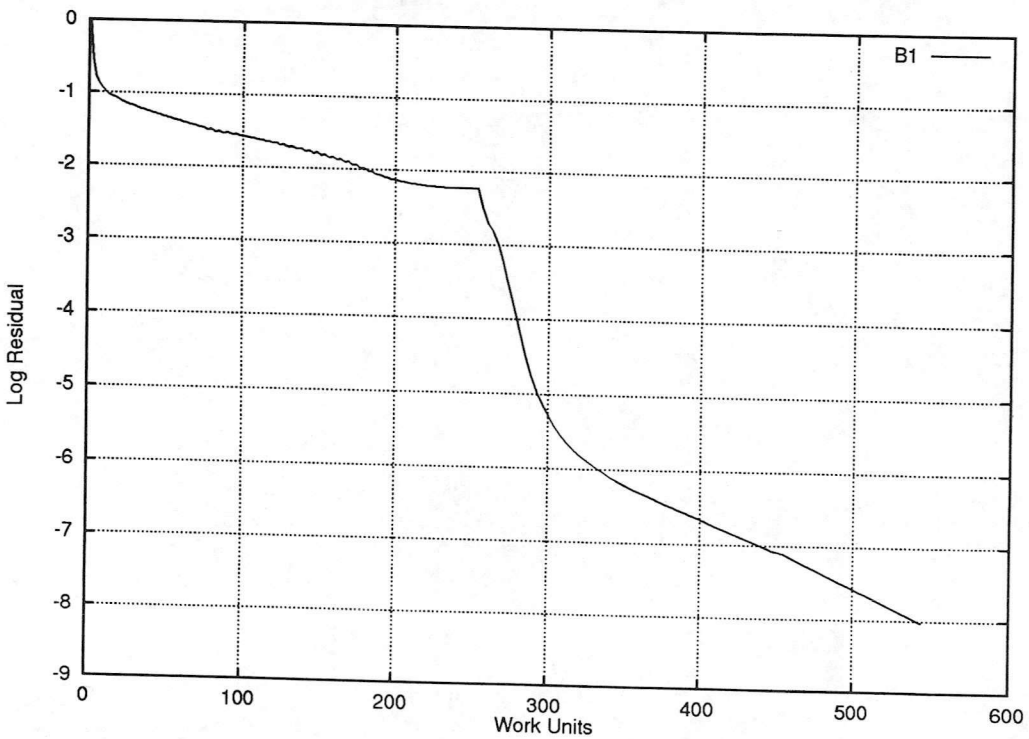


Figure 4.9: *Convergence histories for B1 laminar Navier-Stokes calculation*

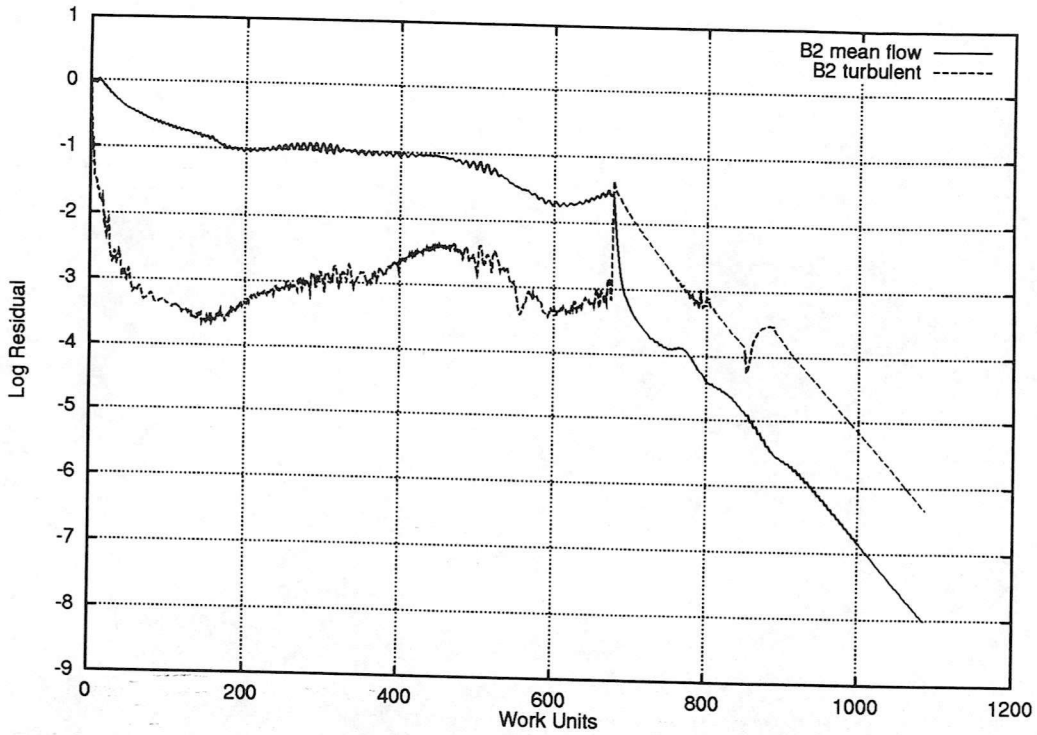


Figure 4.10: *Convergence history for B2 turbulent Navier-Stokes calculation (explicit CFL=0.4)*

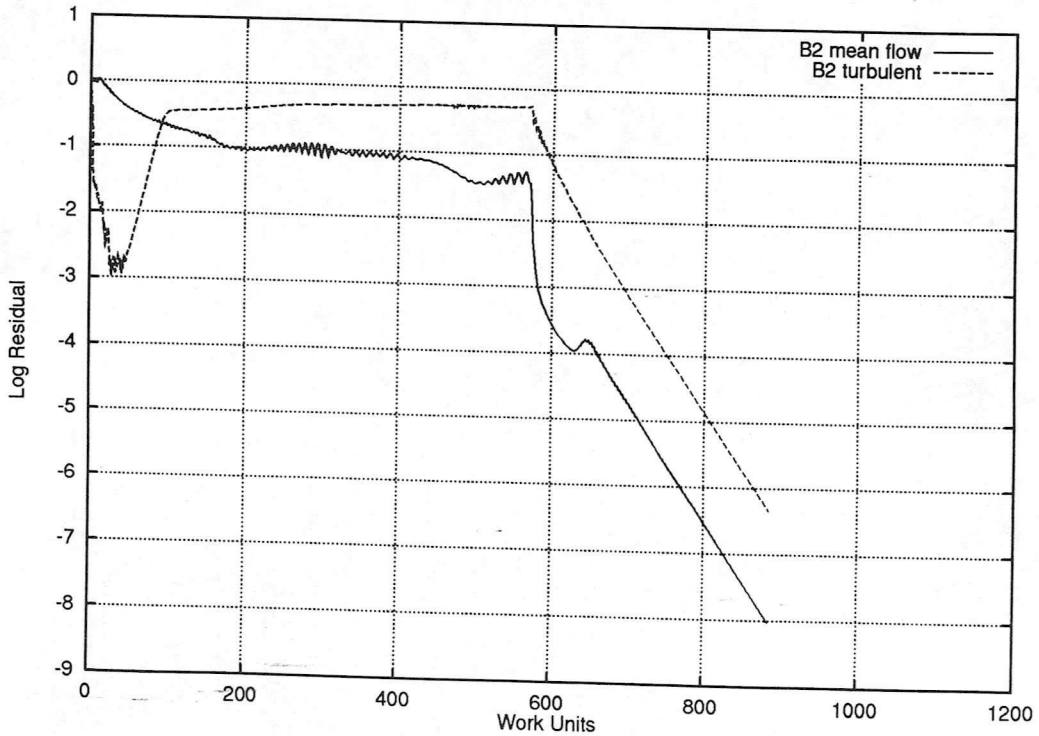


Figure 4.11: *Convergence history for B2 turbulent Navier-Stokes calculation(explicit CFL=0.6)*

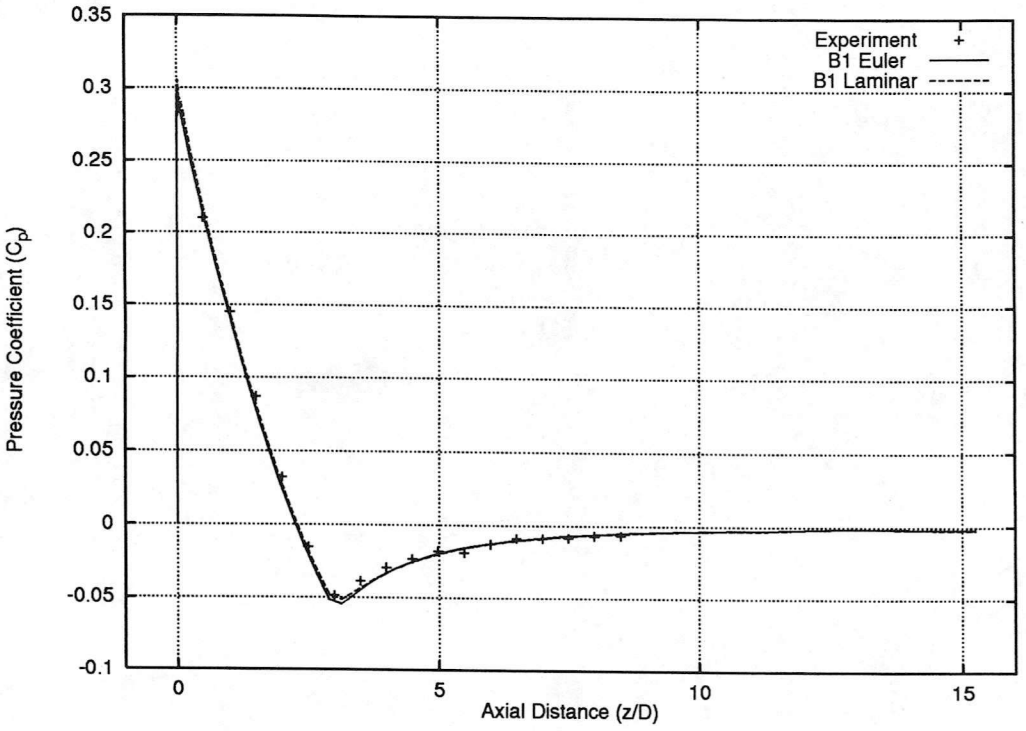


Figure 4.12: *Experimental and calculated pressure coefficient, ONERA B1*

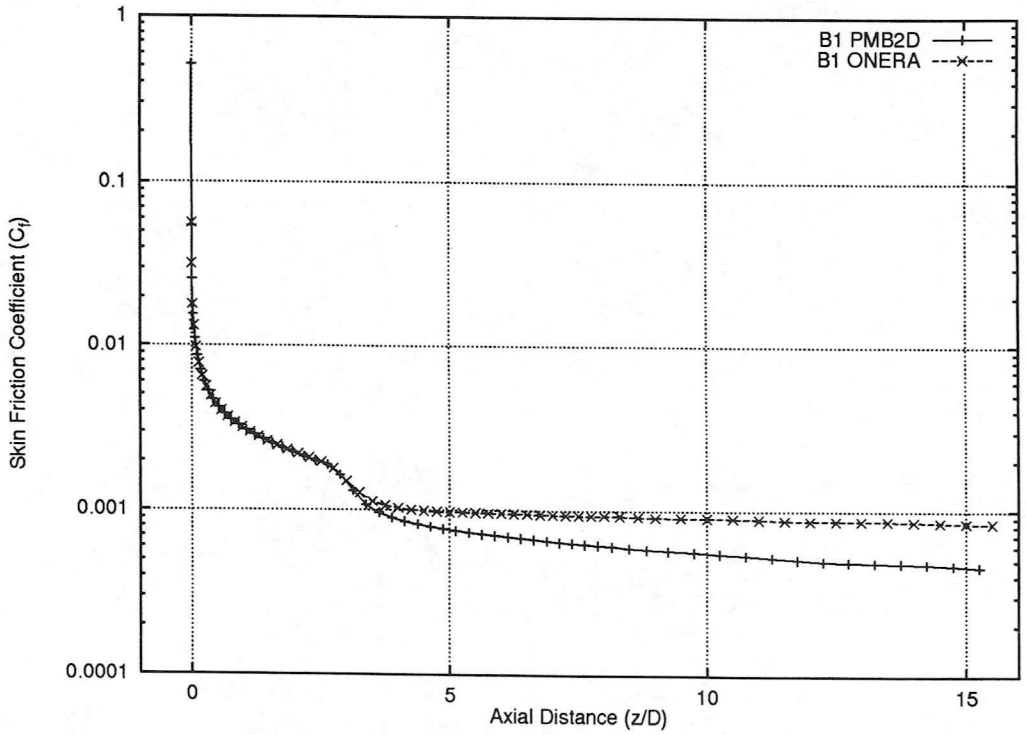


Figure 4.13: *Calculated skin friction coefficient, ONERA B1. (Comparison with ONERA results)*

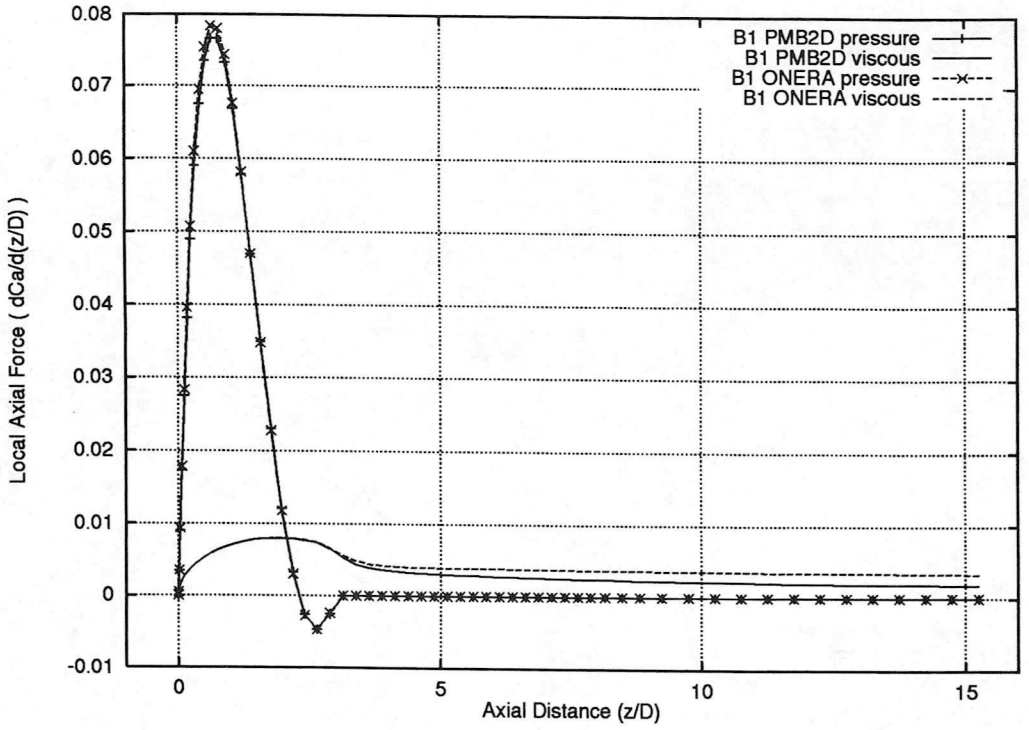


Figure 4.14: *Calculated local axial force coefficient, ONERA B1. (Comparison with ONERA results)*

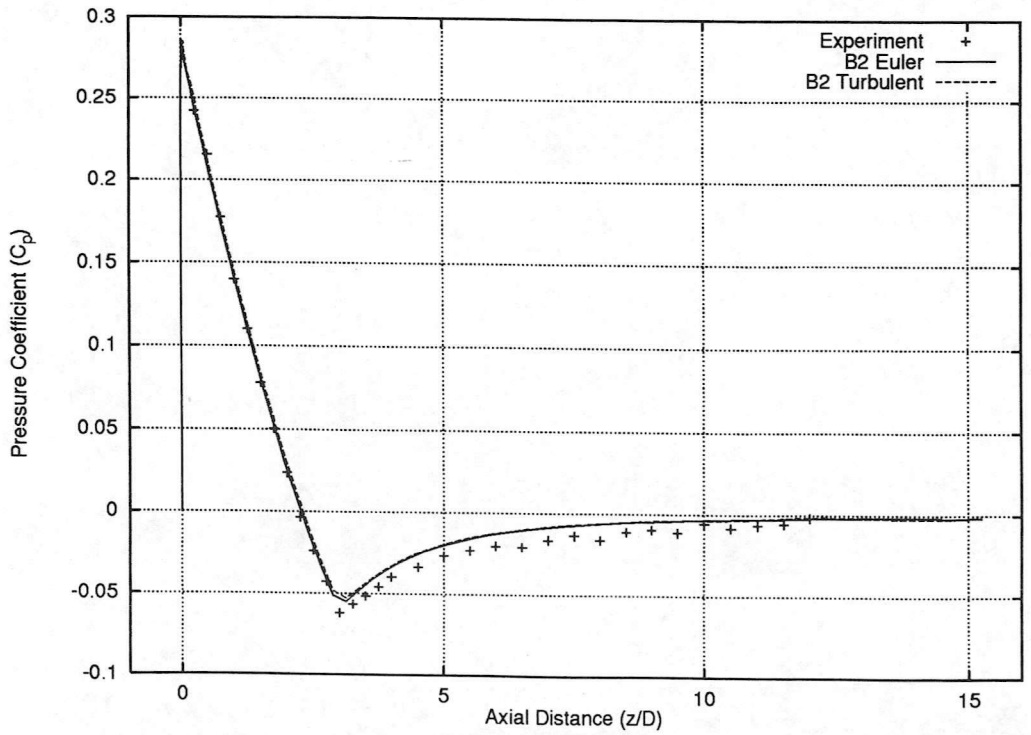


Figure 4.15: *Experimental and calculated pressure coefficient, ONERA B2*

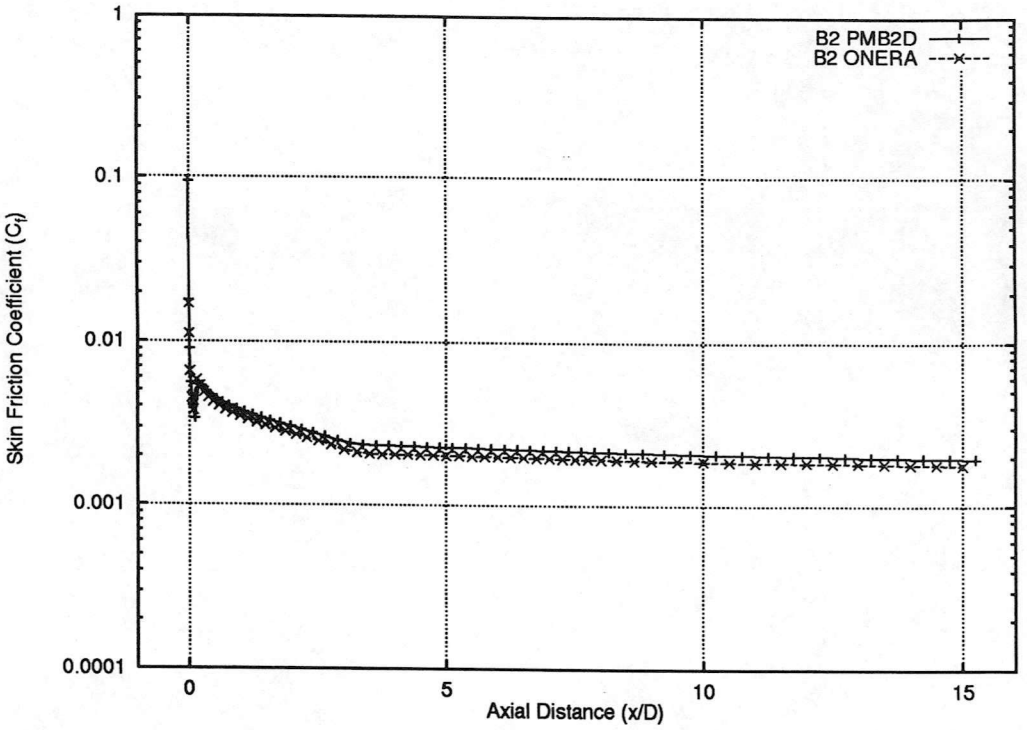


Figure 4.16: *Calculated skin friction coefficient, ONERA B2. (Comparison with ONERA results)*

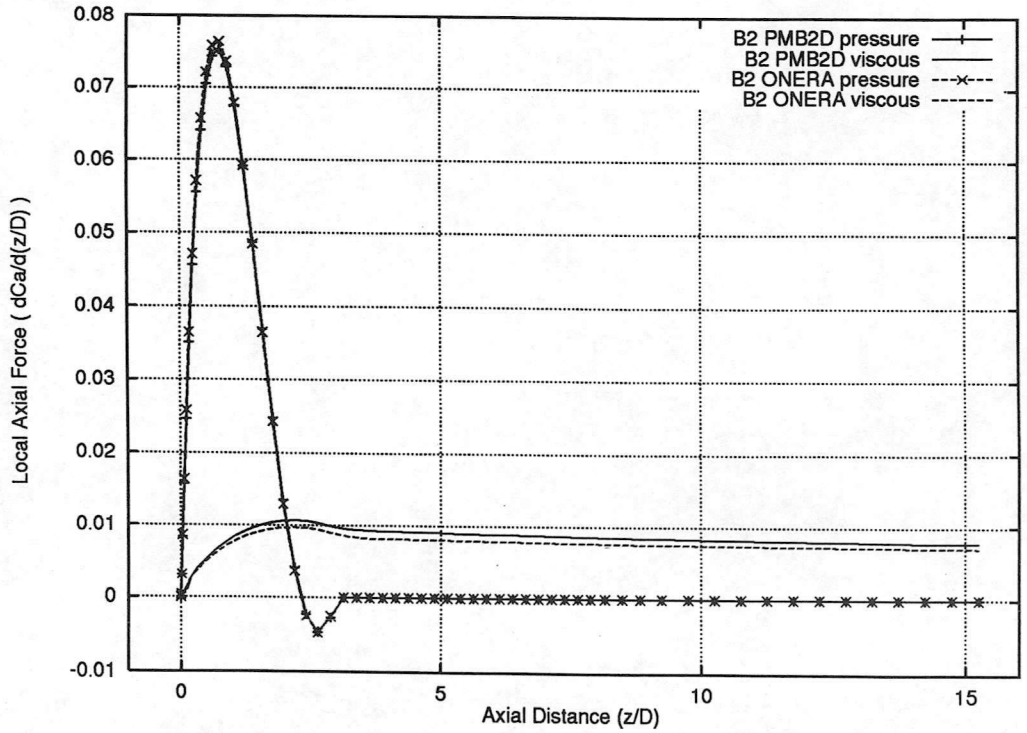


Figure 4.17: *Calculated local axial force coefficient, ONERA B2. (Comparison with ONERA results)*

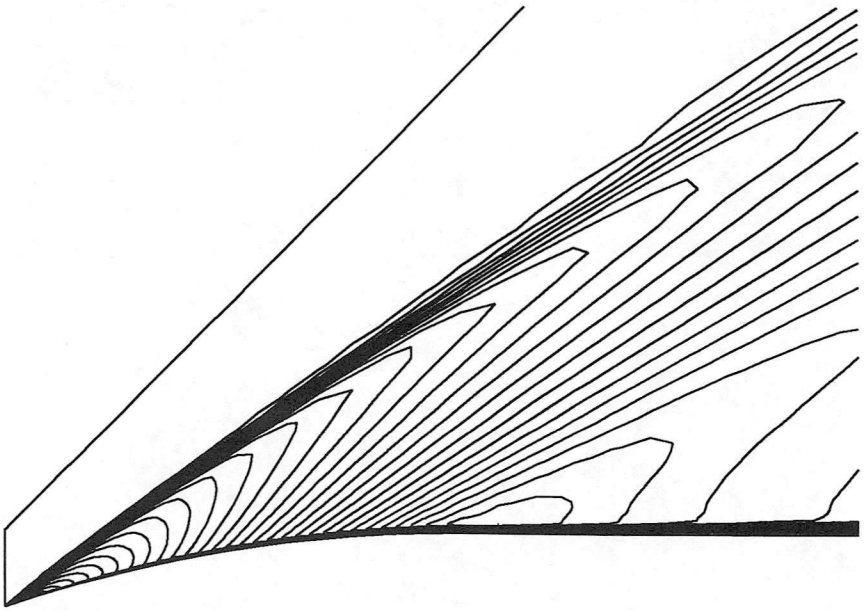

Figure 4.18: *Mach number contours for ONERA B2 test case*

## 4.3 GARTEUR Base Flow

### 4.3.1 Purpose of study

The aerodynamics of the base region strongly influences the drag of a projectile. However, reliable prediction of base flow for the wide range of possible conditions (and geometric configurations) that a designer may wish to examine has still to be attained. Semi-empirical and multi-component methods are very useful in this field but the time-averaged Navier-Stokes approach is the most credible and promising [33], [34]. However, despite the apparent suitability of a Navier-Stokes approach to this type of aerodynamically complex problem results of studies to date have not always been quantitatively satisfactory [33]. Recent studies [6], [7], [35], [36] [37], have indicated the importance of grid generation and turbulence modelling . In particular, the algebraic Baldwin-Lomax turbulence model is dismissed as wholly inappropriate for base flows and the results for $k-\epsilon$ models and variations are better although inconsistent. Some improvement is reported through the use of more sophisticated turbulence models [6]. The present study aims to evaluate the ability of the present method, which uses a $k-\omega$ turbulence model, to provide accurate base flow predictions by examining a test case particularly designed for Navier-Stokes flow solver validation. At the same time the robustness of the present method, the effort required by the engineer in its application and the overall calculation time are kept in mind since accuracy is not the only consideration of the designer operating in a commercial/industrial environment.

### 4.3.2 Description of test case

#### AFTERBODY TEST CASE 1B: CONICAL BOAT-TAIL

The afterbody geometry consists of a short cylindrical section followed by a conical boat-tail at $6^o$ to the cylinder's surface and one cylinder diameter D in length. The geometry and test conditions are described in detail in [38]. The flow conditions are summarised as follows

Fully turbulent flow

$$\begin{aligned} \text{Freestream Mach number, } M_\infty &= 0.35 \\ \text{Reynolds number, } Re_D &= 1.54 * 10^5 \\ \text{Freestream stagnation pressure, } p_{t\infty} &= 10^5 Pa \\ \text{Freestream stagnation temperature, } T_{t\infty} &= 330K \\ \text{Incidence, } \alpha &= 0^o \end{aligned}$$

### 4.3.3 Grid generation

The grids used for previous numerical studies of this test case [34] vary widely in fineness, topology, stretching and far-field boundary extent. In addition, grid convergence checks were absent from these studies. In the present work, the far-field boundary extent was set at the largest values used in the previous studies (15 diameters downstream of the base and 5 diameters normal to the axis of symmetry). In order to determine the number of grid points to use, the number of points in each direction from the coarser grids in [34] was noted, and a grid with four times as many points in each direction was constructed. Successively coarser grids were then obtained by extracting points from this very fine grid, see Table 4.5. This hierarchy of grids formed the basis of the grid convergence study, see Section 4.3.5. The finest grid used here has more than twice as many points as any used in the previous studies. Figure 4.19 shows the coarse grid.

| Number of points | Grids used : a(*very fine*) | b(*fine*) | c(*medium*) | d(*coarse*) |
|---|---|---|---|---|
| Along base | 121 | 61 | 31 | 16 |
| Along boat-tail | 161 | 81 | 41 | 21 |
| Along symmetric line | 281 | 141 | 71 | 36 |
| Normal to symmetric line | 281 | 141 | 71 | 36 |
| Total | 105163 | 26583 | 6793 | 1773 |

Table 4.5: *Summary of grid dimensions*

### 4.3.4 Boundary and initial conditions

The boundary layer thickness at the inflow boundary is included in the report of the experimental results [38]. In order to obtain values to impose at the inflow boundary for the main calculation, a short preliminary calculation was performed using the same conditions on a cylindrical body to simulate the flow upstream of the afterbody. At the axial position where the calculated boundary layer has grown to the reported thickness the values were extracted and used for the inflow condition of the main calculation. All of the flow variables are imposed except the pressure which is extrapolated from the interior since the flow is subsonic. How the inflow boundary condition was tackled in the previous calculations was not included in the respective reports. The conditions at the remaining boundaries are more straightforward. The wall boundary was modelled as being adiabatic with no slip. Symmetry was imposed along the axis of symmetry and a characteristic based far-field boundary condition was employed at the remaining two domain boundaries.

The calculation was initiated from freestream conditions in order to obtain the coarse grid solution. This solution was used as the initial condition for the subsequent medium grid solution and so on. In this way the calculations on the finer grids were initiated from already 'good' conditions thus reducing overall run times.

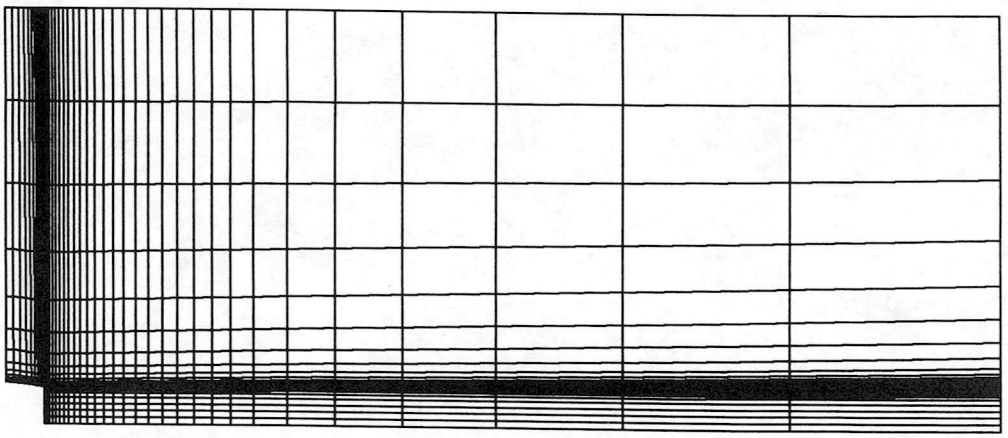

Figure 4.19: *Coarse grid used for GARTEUR afterbody 1B*

### 4.3.5 Results

Results were obtained on the coarse and medium grids without any problem. However, on the two finer grids it was not possible to obtain a solution without altering the turbulence model implementation in an attempt to circumvent an instability problem. The solution would proceed apparently normally before becoming unstable in the vicinity of the free stagnation point and crashing. The initial manifestation of this instability is a sharp increase in the calculated turbulent kinetic energy production term $\hat{\mathbf{P}}_k$ (see Section B.2). A variety of alternative turbulent source term Jacobian matrices, see Section 4.2.6, were implemented in an attempt to improve stability with no success. In order to obtain a solution, the ratio of production to dissipation $\hat{\mathbf{P}}_k/\hat{\mathbf{D}}_k$ was limited. Using the fine and very fine grids the maximum value of this ratio resulting in a stable solution were 1.7 and 1.6 respectively. Note that for the coarser grid calculations (and for calculations on the finer grids employing first-order convective accuracy) this ratio could reach 4.0 in the converged solutions. Figure 4.31 shows a contour plot of this ratio for the solution on the medium grid. The highest values occur at the beginning of the boat-tail on the cylinder, in the free shear layer and in the recirculation region. Imposing a limit on this ratio forces a reduction on the amount of turbulent kinetic energy in the flow and aids stability in the vicinity of the free stagnation point. Note that at the free stagnation point the ratio becomes negative. In addition, a stable solution was also obtained on the fine grid by 'freezing' the turbulent quantities at their values 20 iterations before the failure and continuing to update the mean flow quantities

normally. The justification for this is that before the solution becomes unstable the residuals for the mean flow and turbulent quantities have already decreased by more than three orders of magnitude, the calculation having been initiated from the medium grid solution, so the turbulence field should be a reasonable approximation to the 'real' solution. At the least a solution obtained in this way provides a useful comparison with the solution obtained by using a limit as described above.

Figure 4.20 shows the calculated pressure coefficient distribution along the symmetric line using all four grid levels. The results shown for the fine and very fine grids are those obtained with the production-dissipation limit described above. Figure 4.21 shows how the calculated pressure coefficient distribution along the symmetric line for the 'frozen turbulence' and 'limit' calculations on the fine grid differ slightly. From these figures it is clear that a grid converged solution has not been obtained. It is not possible to blame the differences between the fine and very fine grids solely on the uncertainty caused by the limit used in the calculation. To help indicate whether the grid hierarchy should be sufficient to obtain grid independent results, laminar calculations were also performed. The calculated pressure coefficient distributions along the symmetric line are shown in Figure 4.22. These are also not grid converged. The calculated pressure coefficient along the base compared with experimental data is shown in Figure 4.23. These results again indicate that grid independence has not been achieved and also show poor agreement with experiment. The present pressure coefficient results are similar to the numerical results presented in [34] regarding the location of the maximum and minimum pressures on the symmetric line and generally poor prediction of the base pressure. The present study has strongly indicated the necessity of performing a grid independence study, raising considerable doubt over the validity of computational results obtained without the benefit of such a study even before possible modelling shortcomings are considered. Previous experience and CFD results from other researchers had suggested that the grids used here would be sufficiently fine so the lack of grid independence is disappointing. To complete the study an even finer grid should be used, although solving the instability problems noted above is perhaps a higher priority.

Figures 4.24 to 4.29 show the calculated axial velocity and turbulence kinetic energy profiles for the medium and fine grids compared with experimental data. Figures 4.30 and 4.32 show the calculated pressure and velocity vector field for the medium grid respectively.

The initial calculation performed on the coarse grid took 18 minutes for the residual to converge by 8 orders of magnitude using a Silicon Graphics R5000 processor. The medium and fine grid calculations required 1 hour 17 minutes and 3 hours 20 minutes to converge by 4 orders of magnitude on the same machine. The very fine grid calculation required 6 hours 2 minutes to converge by four orders of magnitude using a 200MHz Intel Pentium Pro processor. The strategy used for obtaining initial conditions is explained in Section 4.3.4. The convergence criteria used here in terms

of residual levels are conservative. The overall execution time for these analyses is therefore very reasonable using widely available desktop computing power. For this case the problem geometry and grid topology are straightforward so the time required for preprocessing should also not be excessive. It is reasonable to conclude that the necessary effort and time required to perform this type of analysis for base flows with the present method should not be restrictive to the design or evaluation engineer.

### 4.3.6 Conclusions

The present method has been applied to an axisymmetric base flow test case designed specifically for the validation of Navier-Stokes flow solvers. The issue of grid convergence has been shown to be very important for this type of flow. Validation of the present approach has been hampered by numerical instability thought to be due to the implicit treatment of the source term in the $k-\omega$ turbulence model. The results which have been obtained are in reasonable agreement with calculations by other researchers. The promise of this type of analysis for base flow problems has been underlined. The potential for relatively inexpensive and fast calculations has been demonstrated.

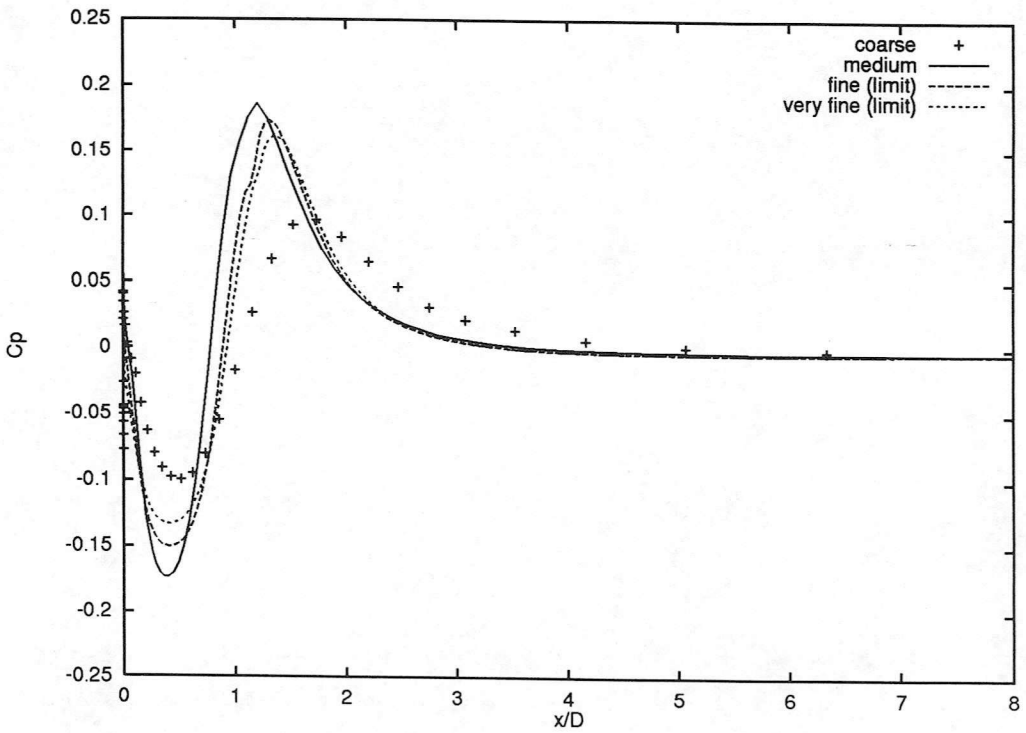


Figure 4.20: *Symmetric line pressure coefficient, 1B*

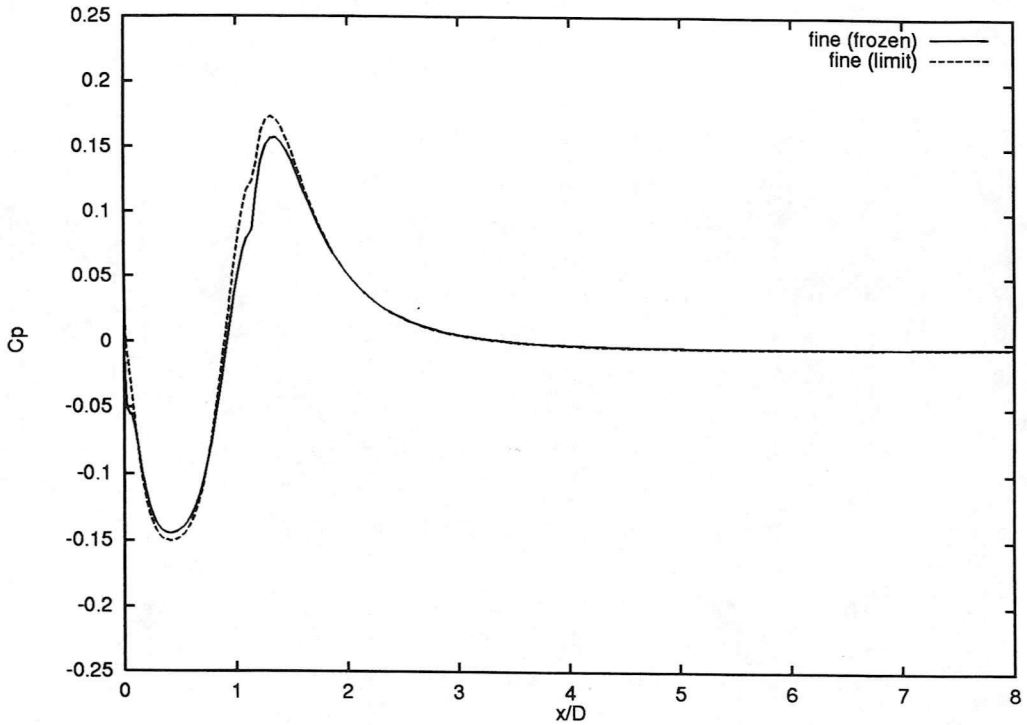


Figure 4.21: *Fine grid results, symmetric line pressure coefficient, 1B*

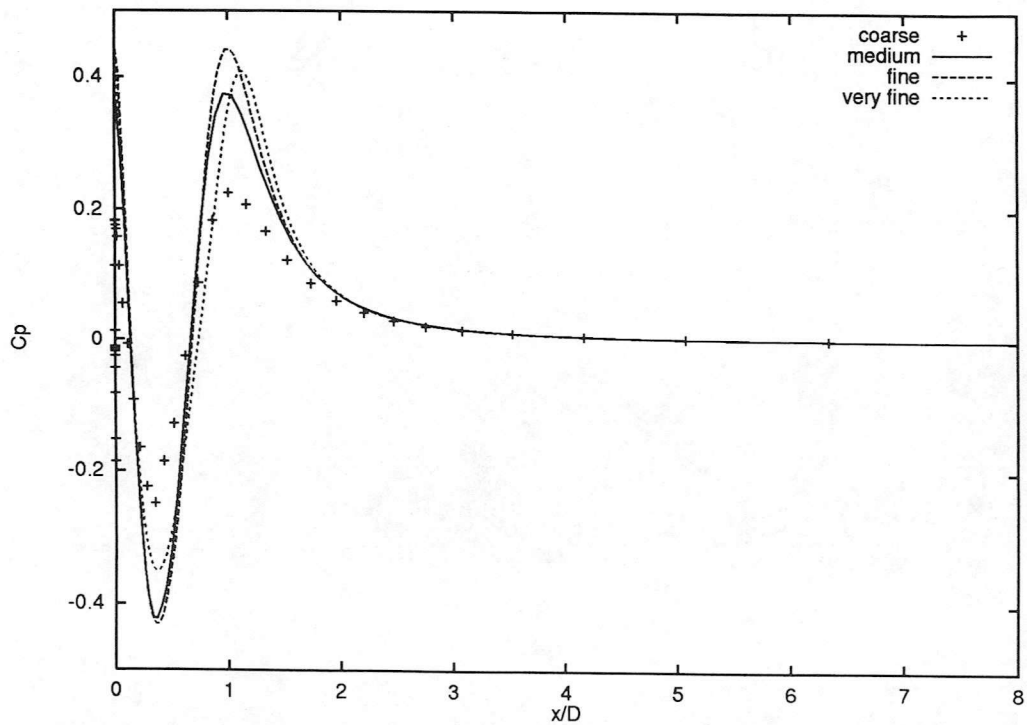


Figure 4.22: *Laminar results, symmetric line pressure coefficient, 1B*

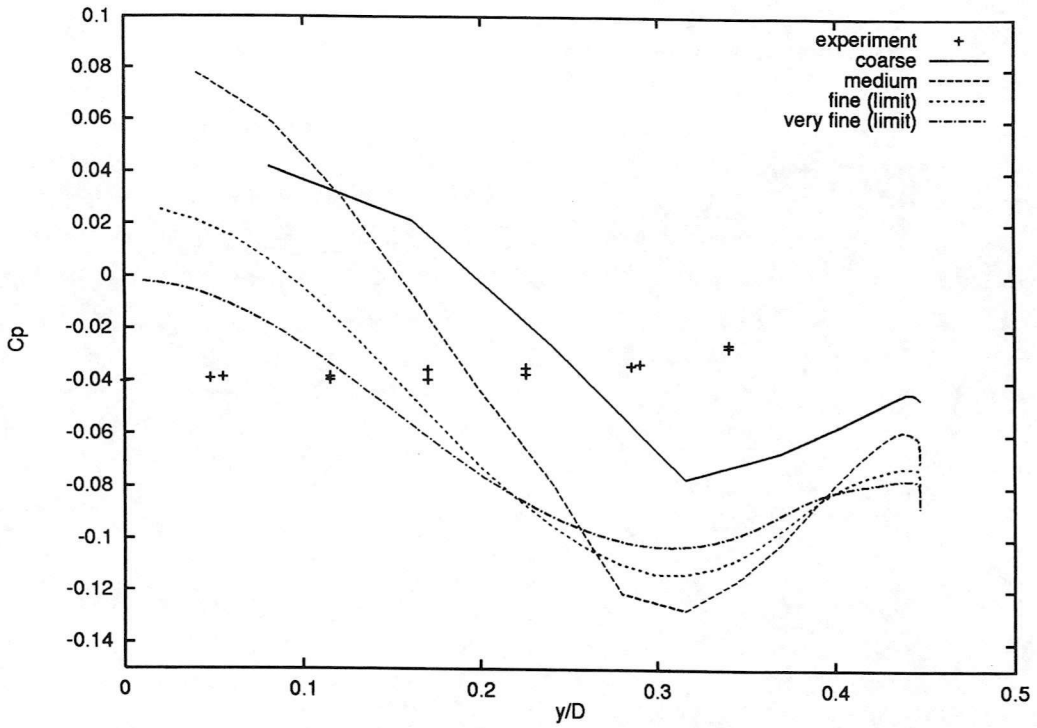


Figure 4.23: *Pressure coefficient along base, 1B*

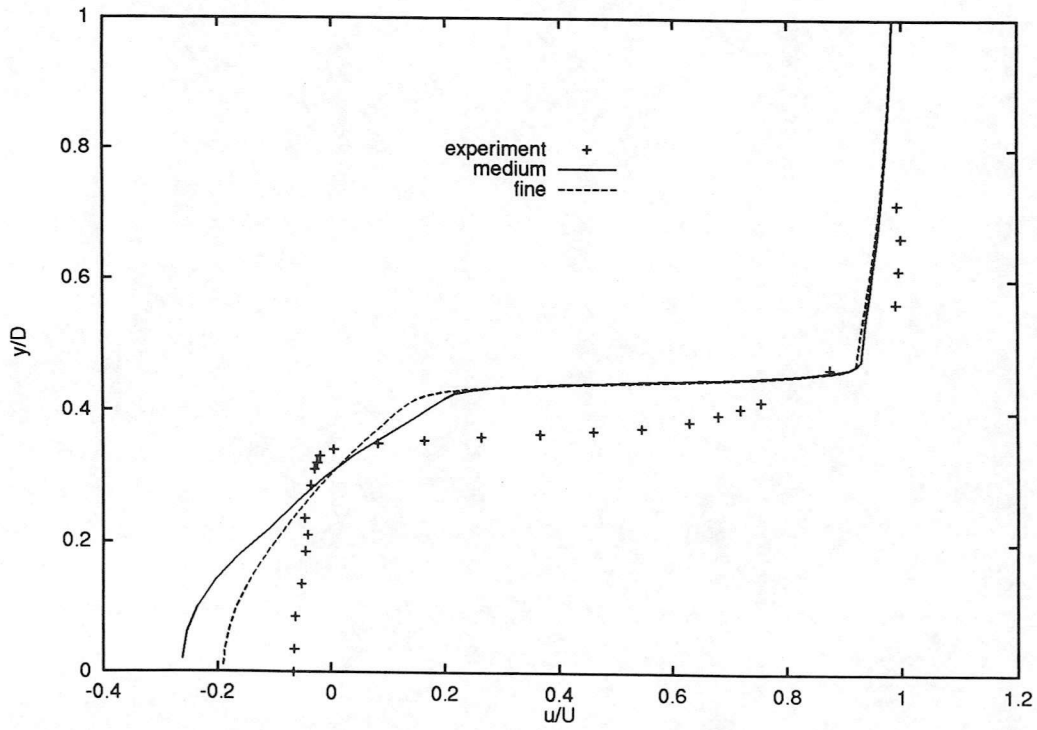


Figure 4.24: *Axial velocity profile at x/D=0.1, 1B*

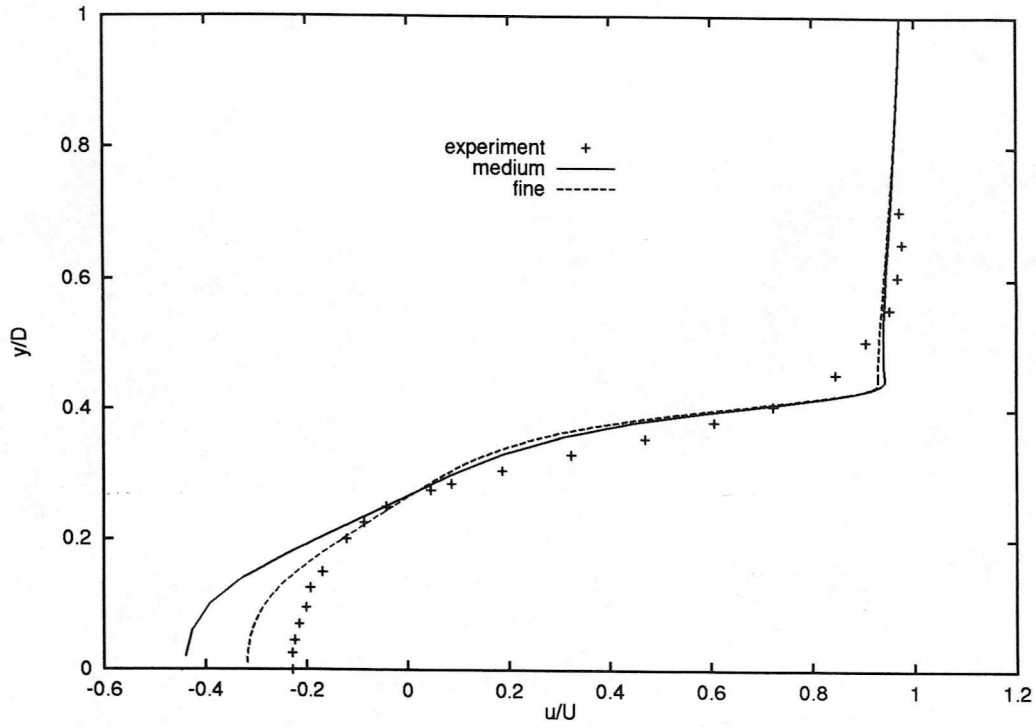


Figure 4.25: *Axial velocity profile at x/D=0.5, 1B*

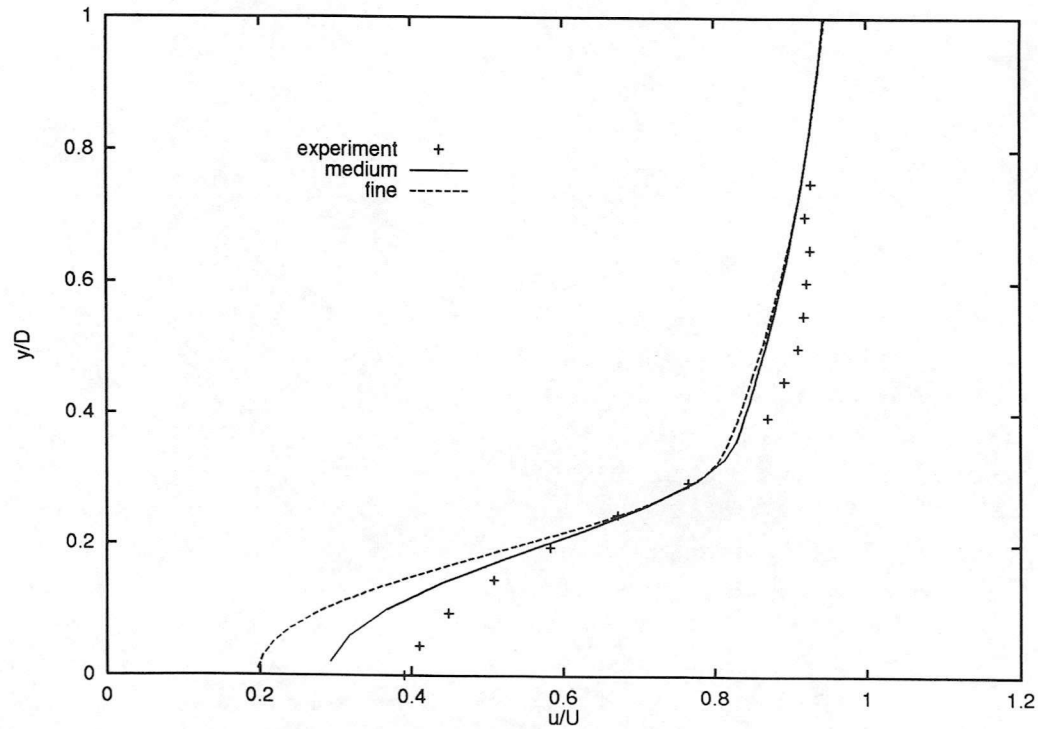


Figure 4.26: *Axial velocity profile at x/D=1.5, 1B*

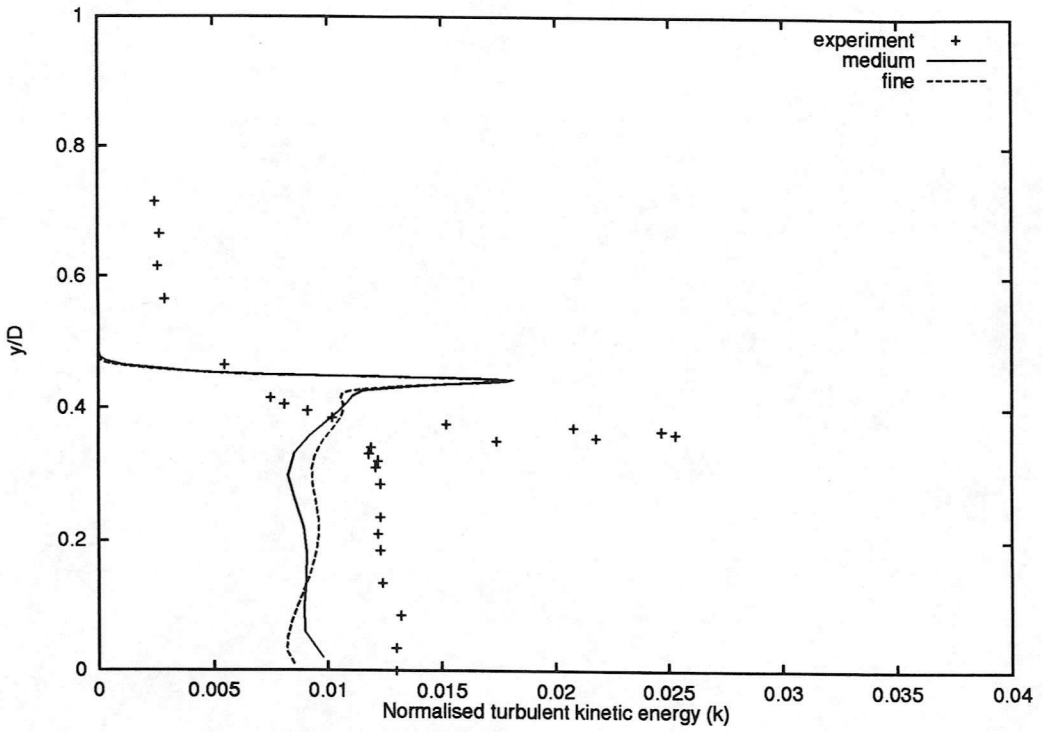


Figure 4.27: *Turbulent kinetic energy profile at x/D=0.1, 1B*

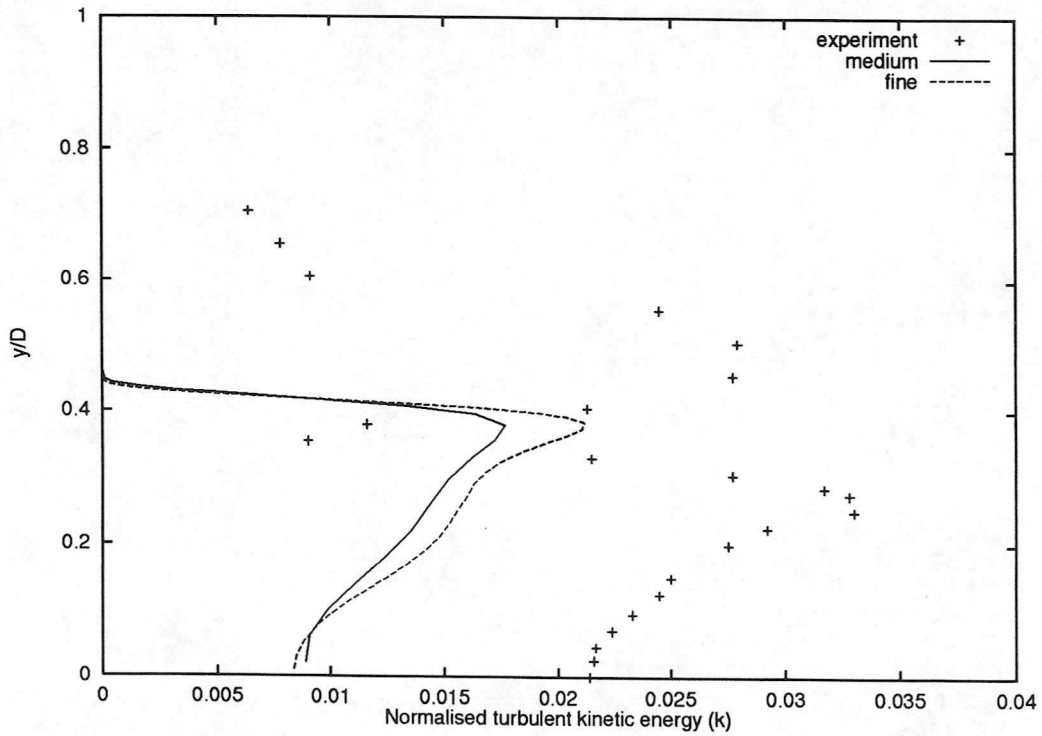


Figure 4.28: *Turbulent kinetic energy profile at x/D=0.5, 1B*

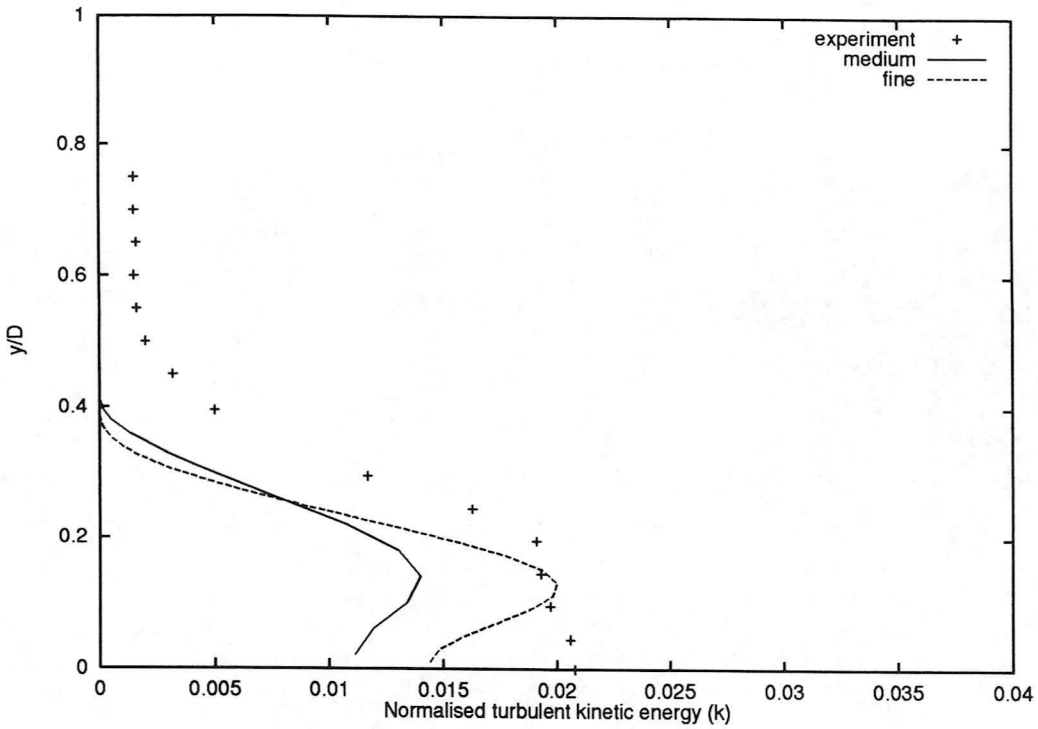


Figure 4.29: *Turbulent kinetic energy profile at x/D=1.5, 1B*

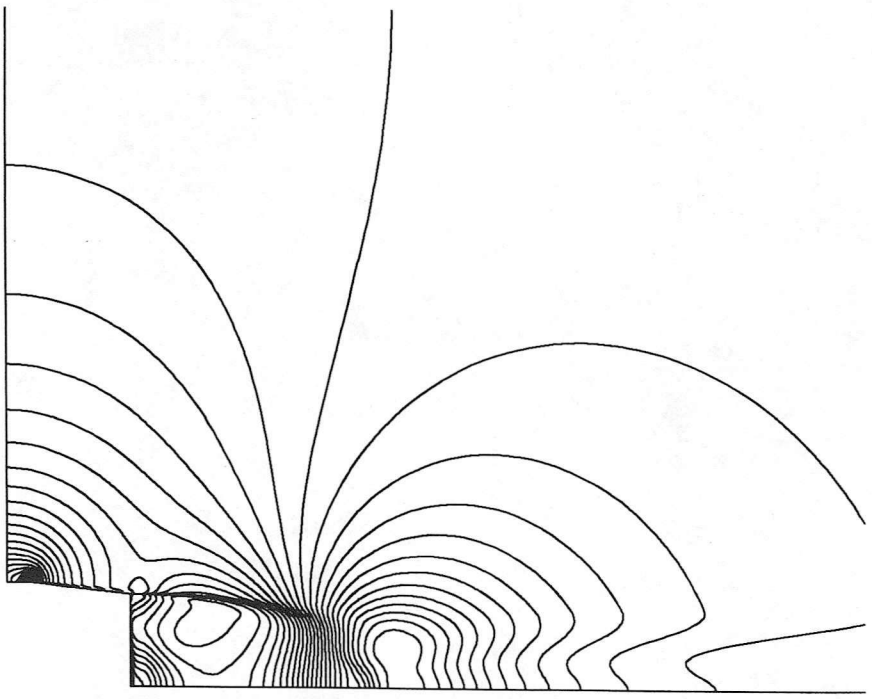

Figure 4.30: *Pressure contours, 1B*

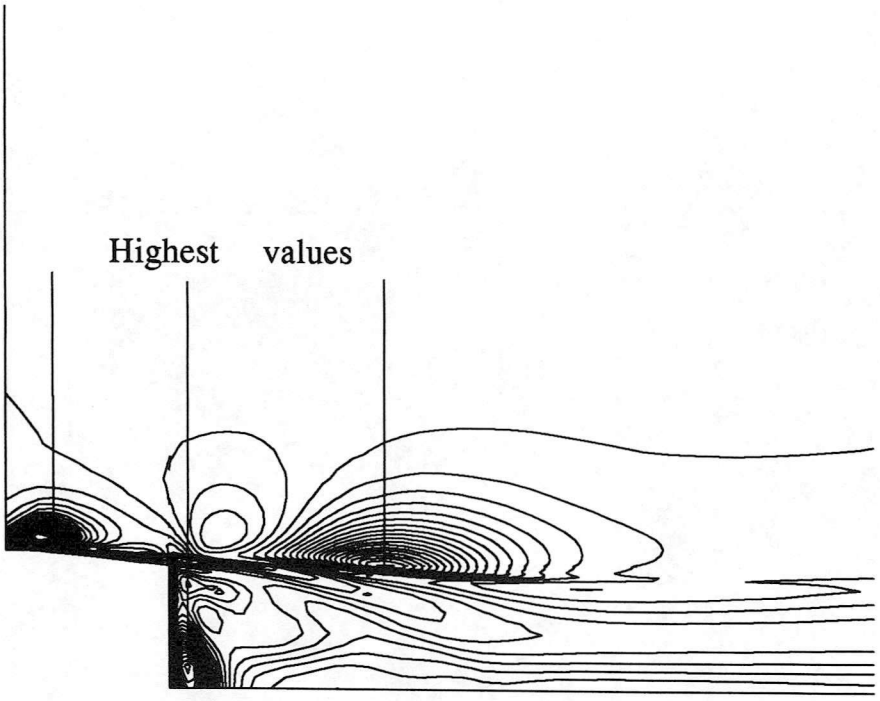


Figure 4.31: $\hat{\mathbf{P}}_k/\hat{\mathbf{D}}_k$ *contours, 1B*

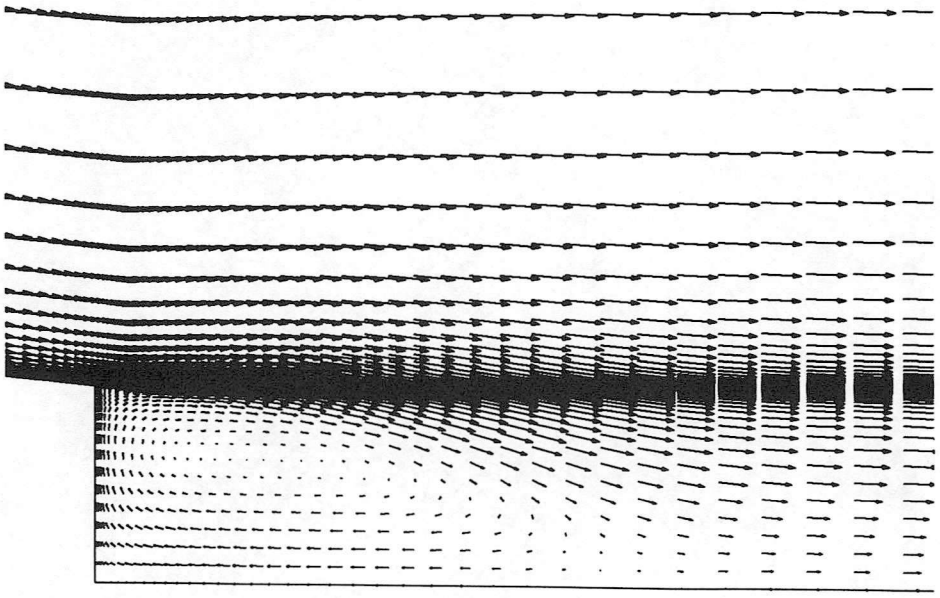

Figure 4.32: *Velocity vectors, 1B*

## 4.4 Discussion

In this chapter the applicability of the present method to aerodynamic problems of interest to industry has been assessed. Test cases representative of two classes of problem, namely missile forebody and base flows, have been examined. It should be noted that other types of problem, for example aerofoil flows, have been examined elsewhere [2], [3], [4].

It has been demonstrated that the present method performs well for supersonic missile forebody calculations involving strong oblique shocks. This conclusion is drawn not only from the results presented in this chapter but also from [32] where a range of forebody geometries and freestream Mach number were considered. The calculations were performed using widely available desktop computing power on a timescale measured in minutes. The B1 Euler case has been examined using a fully three-dimensional version of the present method. The calculation takes approximately 100 times as long and requires 50 times as much memory. The solutions are identical. This clearly demonstrates the utility of an axisymmetric flow solver.

Application of the method to base flow proved more problematic. Although it is still possible to obtain solutions relatively quickly, the method is not robust due to an instability associated with the implementation of the $k-\omega$ turbulence model. Before the method can be applied routinely and with confidence to flows of this type this shortcoming must be redressed. An improved implicit treatment of the turbulent source term may provide the solution to the robustness problem. On a more fundamental level, the deficiencies of two-equation turbulence models including the Boussinesq approximation are well known, see for example [24],[39]. The $k-\omega$ turbulence model gives accurate results for two-dimensional boundary layer flows. However, when the normal components of the Reynolds-stress tensor become non-negligible compared to the shear components, such as in flows with boundary layer separation and sudden changes in shear strain rate, the Boussinesq approximation becomes inaccurate. It is therefore unlikely that close agreement with experiment can be obtained for base flow problems, as seen in the present results. This obvious disadvantage has to be seen in the correct context. Simpler analyses, using semi-empirical methods or CFD with an algebraic turbulence model, give less accurate results in general and/or require case-dependent fine tuning. A CFD analysis employing a more advanced non-linear turbulence model entails prohibitive added complexity.

For axisymmetric problems of this nature a bottleneck in the analysis process often associated with other aerodynamic problems is avoided; grid generation is straightforward due to the relatively simple geometries. An engineer familiar with a structured grid generation tool should be able to construct a grid within a few hours, or modify an existing grid within a few minutes. The post-processing stage of an analysis is now also straightforward due to the wide availability of accomplished

software for this purpose. For missile forebody and base flows the pre- and post-processing associated with the present method should not impede the engineer who requires routine and efficient analyses. For the calculation of axisymmetric forebody flows the present method therefore fulfills the criteria of accuracy and efficiency. Before the present method can be used with the same confidence for base flows further refinement of the numerical method is necessary, although the potential of a Navier-Stokes flow solver for these demanding problems is clear. At present, a standard two-equation turbulence model provides a good balance between accuracy and complexity.

# Appendix A

# The two-dimensional (planar) Navier-Stokes equations

## A.1 Introduction

In this appendix the two-dimensional Navier-Stokes equations are presented in various forms for the sake of completeness and ease of reference to the axisymmetric equations presented in the main body of the report.

## A.2 Non-dimensional form

The derivation of the Navier-Stokes equations is included in most fluid dynamics texts, for example [23]. In a two-dimensional cartesian frame they can be written as

$$\frac{\partial \mathbf{W}}{\partial t} + \frac{\partial (\mathbf{F}^i - \mathbf{F}^v)}{\partial x} + \frac{\partial (\mathbf{G}^i - \mathbf{G}^v)}{\partial y} = 0 \tag{A.1}$$

The vector $\mathbf{W}$ is the vector of conserved variables:

$$\mathbf{W} = \begin{pmatrix} \rho \\ \rho u \\ \rho v \\ \rho E \end{pmatrix} \tag{A.2}$$

where $\rho$ is the density, $\mathbf{V} = (u, v)$ is the Cartesian velocity vector and $E$ is the total energy per unit mass. The flux vectors $\mathbf{F}$ and $\mathbf{G}$ consist of inviscid $(^i)$ and $(^\nu)$ viscous diffusive parts. These are written in full as :

$$\mathbf{F}^i = \begin{pmatrix} \rho u \\ \rho u^2 + p \\ \rho uv \\ \rho uH \end{pmatrix}$$
$$\mathbf{G}^i = \begin{pmatrix} \rho v \\ \rho uv \\ \rho v^2 + p \\ \rho vH \end{pmatrix} \tag{A.3}$$

$$\mathbf{F}^\nu = \frac{1}{Re} \begin{pmatrix} 0 \\ \tau_{xx} \\ \tau_{xy} \\ u\tau_{xx} + v\tau_{xy} + q_x \end{pmatrix}$$
$$\mathbf{G}^\nu = \frac{1}{Re} \begin{pmatrix} 0 \\ \tau_{xy} \\ \tau_{yy} \\ u\tau_{xy} + v\tau_{yy} + q_y \end{pmatrix} \tag{A.4}$$

The stress tensor and of the heat flux vector components are written as:

$$\begin{aligned} \tau_{xx} &= -\mu \left( 2\frac{\partial u}{\partial x} - \frac{2}{3}\left( \frac{\partial u}{\partial x} + \frac{\partial v}{\partial y} \right) \right) \\ \tau_{yy} &= -\mu \left( 2\frac{\partial v}{\partial y} - \frac{2}{3}\left( \frac{\partial u}{\partial x} + \frac{\partial v}{\partial y} \right) \right) \\ \tau_{xy} &= -\mu \left( \frac{\partial u}{\partial y} + \frac{\partial v}{\partial x} \right) \\ q_x &= -\frac{1}{(\gamma - 1)M_\infty^2} \frac{\mu}{Pr} \frac{\partial T}{\partial x} \\ q_y &= -\frac{1}{(\gamma - 1)M_\infty^2} \frac{\mu}{Pr} \frac{\partial T}{\partial y} \end{aligned} \tag{A.5}$$

Here $\gamma$ is the specific heat ratio, $Pr$ is the laminar Prandtl number, $T$ is the static temperature and $M_\infty$ and $Re$ are the freestream Mach number and Reynolds number, respectively. The various flow quantities are related to each other by the perfect gas relations:

$$\begin{aligned} H &= E + \frac{p}{\rho} \\ E &= e + \frac{1}{2}\left(u^2 + v^2\right) \\ p &= (\gamma - 1)\,\rho e \\ \frac{p}{\rho} &= \frac{T}{\gamma M_\infty^2} \end{aligned} \tag{A.6}$$

Finally, the laminar viscosity $\mu$ is evaluated using Sutherland's law:

$$\frac{\mu}{\mu_0} = \left(\frac{T}{T_0}\right)^{3/2} \frac{T_0 + 110}{T + 110} \tag{A.7}$$

where $\mu_0$ is a reference viscosity at a reference temperature $T_0$. These can be taken as $\mu_0 = 1.7894\text{x}10^{-5}$ kg/(m.s) with $T_0 = 288.16$ K. It is stressed that the quantities presented here have been non-dimensionalised. The procedure used is as follows:

$$x = \frac{x^*}{L^*}, \qquad y = \frac{y^*}{L^*}, \qquad t = \frac{t^*}{L^*/V_\infty^*},$$

$$u = \frac{u^*}{V_\infty^*}, \qquad v = \frac{v^*}{V_\infty^*}, \qquad \mu = \frac{\mu^*}{\mu_\infty^*},$$

$$\rho = \frac{\rho^*}{\rho_\infty^*}, \qquad p = \frac{p^*}{p_\infty^* V_\infty^{*2}}, \qquad T = \frac{T^*}{T_\infty^*}, \qquad e = \frac{e^*}{V_\infty^{*2}} \tag{A.8}$$

## A.3 Reynolds-averaged form

The Reynolds-averaged form of the Navier-Stokes equations permits turbulent flow to be considered. The development is not presented here. It is merely noted that fundamental to this approach is the consideration of the flow variables as consisting of two components, a time averaged component and a turbulent fluctuation component. For example, density and velocity components are decomposed as

$$u = \bar{u} + u', \qquad v = \bar{v} + v', \qquad \rho = \bar{\rho} + \rho'$$

The quantities $k$ (the turbulent kinetic energy), $\mu_T$ (the turbulent viscosity) and $Pr_T$ (the turbulent Prandtl number) are introduced via the important Boussinesq assumption in an attempt to model the fluctuating-variable stress terms arising from the Reynolds averaging. For a complete discussion of this subject see [23]. The Reynolds-averaged form of the Navier-Stokes equations are identical to those presented in appendix A.2, except for the stress tensor and heat flux vector components shown below. The variables should be considered as mean flow quantities (superscripts are dropped for clarity). The turbulent nature of the flow is modelled via $\mu_T$ and $k$ and a closure hypothesis or turbulence model, for example the $k-\omega$ model, appendix B.

$$\begin{aligned}
\tau_{xx} &= -(\mu+\mu_T)\left(2\frac{\partial u}{\partial x}-\frac{2}{3}\left(\frac{\partial u}{\partial x}+\frac{\partial v}{\partial y}\right)\right)+\frac{2}{3}\rho k \\
\tau_{yy} &= -(\mu+\mu_T)\left(2\frac{\partial v}{\partial y}-\frac{2}{3}\left(\frac{\partial u}{\partial x}+\frac{\partial v}{\partial y}\right)\right)+\frac{2}{3}\rho k \\
\tau_{xy} &= -(\mu+\mu_T)\left(\frac{\partial u}{\partial y}+\frac{\partial v}{\partial x}\right) \qquad \text{(A.9)} \\
q_x &= -\frac{1}{(\gamma-1)M_\infty^2}\left(\frac{\mu}{Pr}+\frac{\mu_T}{Pr_T}\right)\frac{\partial T}{\partial x} \\
q_y &= -\frac{1}{(\gamma-1)M_\infty^2}\left(\frac{\mu}{Pr}+\frac{\mu_T}{Pr_T}\right)\frac{\partial T}{\partial y} \qquad \text{(A.10)}
\end{aligned}$$

## A.4 Curvilinear form

The governing equations are written in curvilinear $(\xi,\eta)$ form to facilitate use on curvilinear grids of arbitrary local orientation and density. A space transformation from the Cartesian coordinate system to the local coordinate system must then be introduced:

$$\begin{aligned}
\xi &= \xi(x,y) \\
\eta &= \eta(x,y) \\
t &= t
\end{aligned}$$

The Jacobian matrix of the transformation is given by

$$J = \frac{\partial(\xi,\eta)}{\partial(x,y)}$$

The equations A.1 can then be written as

$$\frac{\partial \hat{\mathbf{W}}}{\partial t}+\frac{\partial(\hat{\mathbf{F}}^i-\hat{\mathbf{F}}^v)}{\partial \xi}+\frac{\partial(\hat{\mathbf{G}}^i-\hat{\mathbf{G}}^v)}{\partial \eta}=0 \qquad \text{(A.11)}$$

where

$$\begin{aligned}
\hat{\mathbf{W}} &= \frac{\mathbf{W}}{J} \\
\hat{\mathbf{F}}^i &= \frac{1}{J}\left(\xi_x \mathbf{F}^i + \xi_y \mathbf{G}^i\right) \\
\hat{\mathbf{G}}^i &= \frac{1}{J}\left(\eta_x \mathbf{F}^i + \eta_y \mathbf{G}^i\right) \\
\hat{\mathbf{F}}^v &= \frac{1}{J}\left(\xi_x \mathbf{F}^v + \xi_y \mathbf{G}^v\right) \\
\hat{\mathbf{G}}^v &= \frac{1}{J}\left(\eta_x \mathbf{F}^v + \eta_y \mathbf{G}^v\right)
\end{aligned} \tag{A.12}$$

The expressions for the inviscid fluxes can be simplified somewhat by defining

$$\begin{aligned}
U &= \xi_x u + \xi_y v \\
V &= \eta_x u + \eta_y v
\end{aligned} \tag{A.13}$$

The inviscid fluxes can then be written as

$$\begin{aligned}
\hat{\mathbf{F}}^i &= \begin{pmatrix} \rho U \\ \rho u U + \xi_x p \\ \rho v U + \xi_y p \\ \rho U H \end{pmatrix} \\
\hat{\mathbf{G}}^i &= \begin{pmatrix} \rho V \\ \rho u V + \eta_x p \\ \rho v V + \eta_y p \\ \rho V H \end{pmatrix}
\end{aligned} \tag{A.14}$$

The derivative terms found in the viscous fluxes are evaluated using the chain rule, for example

$$\frac{\partial u}{\partial x} = \xi_x \frac{\partial u}{\partial \xi} + \eta_x \frac{\partial u}{\partial \eta}$$

The evaluation of the metrics of the transformation is clearly important, and is described in full in [23].

# Appendix B

# The two-equation $k-\omega$ turbulence model

## B.1 Non-dimensional form

The $k-\omega$ turbulence model of Wilcox [24] in non-dimensional form can be written as follows:

**Eddy Viscosity**

$$\mu_T = \rho k/\omega \tag{B.1}$$

**Turbulence Kinetic Energy**

$$\rho\frac{\partial k}{\partial t} + \rho\mathbf{V}.\nabla k - \frac{1}{Re}\nabla.\left[\left(\mu + \sigma^*\mu_T\right)\nabla k\right] = \mu_T P - \frac{2}{3}\rho k S - \beta^*\rho k\omega \tag{B.2}$$

**Specific Dissipation Rate**

$$\rho\frac{\partial \rho\omega}{\partial t} + \rho\mathbf{V}.\nabla\omega - \frac{1}{Re}\nabla.\left[\left(\mu + \sigma\mu_T\right)\nabla\omega\right] = \alpha\frac{\omega}{k}\left[\mu_T P - \frac{2}{3}\rho k S\right] - \beta\rho\omega^2 \tag{B.3}$$

**Closure Coefficients**

$$\alpha = 5/9, \qquad \beta = 3/40, \qquad \beta^* = 9/100, \qquad \sigma = 1/2, \qquad \sigma^* = 1/2 \tag{B.4}$$

In the above relations,

$$\begin{aligned} P &= \left[\left(\nabla\mathbf{V} + \nabla\mathbf{V}^T\right) : \nabla\mathbf{V} - \frac{2}{3}\left(\nabla.\mathbf{V}\right)^2\right] \\ S &= \nabla.\mathbf{V} \end{aligned}$$

The equations as shown above use the same non-dimensional quantities as in section section A.2, with the addition of

$$k = \frac{k^* Re}{V_\infty^{*2}}, \qquad \omega = \frac{\omega^* L^*}{V_\infty^*}, \qquad \mu_T = \frac{\mu_T^*}{\mu_\infty^*}$$

## B.2 Curvilinear form

The equations for $k$ and $\omega$ can be written in a curvilinear form analogous to that used for the mean flow equations in section A.4 . Written in full, the two-dimensional Cartesian form of equations B.3 and B.4 become

$$\frac{\partial \hat{\mathbf{W}}_T}{\partial t} + \frac{\partial(\hat{\mathbf{F}}_T^i - \hat{\mathbf{F}}_T^v)}{\partial \xi} + \frac{\partial(\hat{\mathbf{G}}_T^i - \hat{\mathbf{G}}_T^v)}{\partial \eta} = \frac{\hat{\mathbf{S}}_T}{J} \tag{B.5}$$

where the vectors of conserved variables, convective and diffusive fluxes are respectively

$$\hat{\mathbf{W}}_T = \frac{1}{J}\begin{pmatrix} \rho k \\ \rho \omega \end{pmatrix} \qquad \hat{\mathbf{F}}_T^i = \frac{1}{J}\begin{pmatrix} \rho k U \\ \rho \omega U \end{pmatrix} \qquad \hat{\mathbf{G}}_T^i = \frac{1}{J}\begin{pmatrix} \rho k V \\ \rho \omega V \end{pmatrix}$$

$$\hat{\mathbf{F}}_T^v = \frac{1}{J}\left(\xi_x \hat{\mathbf{M}} + \xi_y \hat{\mathbf{N}}\right) \qquad \hat{\mathbf{G}}_T^v = \frac{1}{J}\left(\eta_x \hat{\mathbf{M}} + \eta_y \hat{\mathbf{N}}\right)$$

where the tensors M and N are equal to

$$\hat{\mathbf{M}} = \frac{1}{Re}\begin{pmatrix} (\mu + \sigma^* \mu_T)(\xi_x k_\xi + \eta_x k_\eta) \\ (\mu + \sigma \mu_T)(\xi_x \omega_\xi + \eta_x \omega_\eta) \end{pmatrix}$$

$$\hat{\mathbf{N}} = \frac{1}{Re}\begin{pmatrix} (\mu + \sigma^* \mu_T)(\xi_y k_\xi + \eta_y k_\eta) \\ (\mu + \sigma \mu_T)(\xi_y \omega_\xi + \eta_y \omega_\eta) \end{pmatrix}$$

Finally, the source term is written as

$$\hat{\mathbf{S}}_T = \begin{pmatrix} \hat{\mathbf{P}}_k - \hat{\mathbf{D}}_k \\ \hat{\mathbf{P}}_\omega - \hat{\mathbf{D}}_\omega \end{pmatrix}$$

with the components

$$\hat{\mathbf{P}}_k = \mu_T \left\{ \left( \frac{\partial u}{\partial y} + \frac{\partial v}{\partial x} \right)^2 + 2 \left[ \left( \frac{\partial u}{\partial x} \right)^2 + \left( \frac{\partial v}{\partial y} \right)^2 \right] - \frac{2}{3} \left( \frac{\partial u}{\partial x} + \frac{\partial v}{\partial y} \right)^2 \right\} - \frac{2}{3} \rho k \left( \frac{\partial u}{\partial x} + \frac{\partial v}{\partial y} \right)$$

$$\hat{\mathbf{D}}_k = \beta^* \rho \omega k$$

$$\hat{\mathbf{P}}_\omega = \alpha \frac{\omega}{k} \hat{\mathbf{P}}_k$$

$$\hat{\mathbf{D}}_\omega = \beta \rho \omega^2$$

Again the velocity derivative terms are evaluated in $(\xi,\eta)$ space via the chain rule, as mentioned in section A.4, but remain unexpanded in the source term components above for brevity.

# Bibliography


[1] K.J. Badcock, W. McMillan, M.A. Woodgate, B.J. Gribben, S. Porter and B.E. Richards. Integration of an Implicit Multiblock Code into a Workstation Cluster Environment. In P. Schiano et al., editor, *Parallel Computational Fluid Dynamics: Algorithms and Results using Advanced Computers*, pages 408–415. Elsevier Science B.V. Amsterdam, 1996.

[2] F. Cantariti, L. Dubuc, B.J. Gribben, M. Woodgate, K.J. Badcock and B.E. Richards. Approximate Jacobians for the Euler and Navier-Stokes Equations. *University of Glasgow, Aero Report 9705*, 1997.

[3] L. Dubuc, F. Cantariti, M. Woodgate, B.J. Gribben, K.J. Badcock and B.E. Richards. Solution of the Euler unsteady equations using deforming grids. *University of Glasgow, Aero Report 9704*, 1997.

[4] R.M. Gatiganti, K.J. Badcock, F. Cantariti, L. Dubuc, M. Woodgate and B.E. Richards. Evaluation of an Unfactored Method for the Solution of the Incompressible Flow Equations using Artificial Compressibility. *Applied Ocean Research (accepted for publication)*, 1998.

[5] J. Sahu, C.J. Nietubicz and J.L. Steger. Navier-Stokes Computations of Projectile Base Flow with and without Mass Injection. *AIAA Journal*, 23(9):1348–1355, 1985.

[6] C.C. Chuang and C.C. Chieng. Supersonic Base-Flow Computation Using Higher-Order Closure Turbulence Models. *Journal of Spacecraft and Rockets*, 33(3):374–380, 1996.

[7] R.E. Childs and S.C. Caruso. Assessment of Modeling and Discretization Accuracy for High-Speed Afterbody Flows. *Journal of Propulsion*, 7(4):607–616, 1991.

[8] F. Magagnato. Computation of Axisymmetric Base Flow with Different Turbulence Models. In *AGARD-CP-493, Missile Aerodynamics*, 1990.

[9] C. Vassilopoulus, K.C. Giannakoglou and K.D. Papailiou. Supersonic Rearward-Facing Step Calculations Using an Explicit Fractional-step Method and a Two-Equation Turbulence Model. In *ETMA Workshop on Turbulence Modelling for Compressible Flow arising on Aeronautics*, 1994.

[10] British Aerospace contribution, Action Group 09. Flow past Missile Afterbodies. In *GARTEUR TP no. 061*, pages 137–144, November 1991.

[11] Matra Defense contribution, Action Group 09. Flow past Missile Afterbodies. In *GARTEUR TP no. 061*, pages 156–160, November 1991.

[12] M-H. Chen, C-C. Hsu and W. Shyy. Assessment of TVD Schemes for Inviscid and Turbulent Flow Computation. *International Journal for Numerical Methods in Fluids*, 12:161–177, 1991.

[13] R.C-C. Luh and C.K. Lombard. Projectile Aerodynamics Prediction with CSCM-S Upwind Implicit Relaxation Algorithm. *AIAA-85-1838*, 1985.

[14] K.J. Moran and P.S. Beran. Navier-Stokes Simulations of Slender Axisymmetric Shapes in Supersonic, Turbulent Flow. *AIAA Journal*, 32(7):1446–1456, 1994.

[15] P.D. Orkwiss and D.S. McRae. Newton's Method for the Axisymmetric Navier-Stokes Equations. *AIAA Journal*, 30(6):1507–1514, 1992.

[16] E. Weide, E.Issman, H.Deconinck and G.Degrez. A Parallel Implicit Multidimensional Upwind Cell Vertex Navier-Stokes Solver for Hypersonic Applications. In *AGARD-R-813, Aerothermodynamics and Propulsion Integration for Hypersonic Vehicles*, 1996.

[17] S.S. Gokhale and R. Suresh. Numerical Computations of Internal Flows for Axisymmetric and Two-dimensional Nozzles. *International Journal for Numerical Methods in Fluids*, 25(5):599–610, September 1997.

[18] B.J. Gribben, K.J. Badcock and B.E. Richards. Shock Reflection Hysteresis in an Underexpanded Jet: a CFD Study. *University of Glasgow, Aero Report 9808*, 1998.

[19] P. Glaister. Flux Difference Splitting for the Euler Equations with Axial Symmetry. *Journal of Engineering Mathematics*, 22:107–121, 1988.

[20] C. Hirsch. *Fundamentals of Numerical Discretisation*, volume 1. Numerical Computation of Internal and External Flows, John Wiley, 1990.

[21] J.H. Heinbockel. *Tensor Analysis and Continuum Mechanics.* Old Dominion University, `http://www.math.odu.edu/~jhh/johnh.html`, 1996.

[22] S. Eskinazi. *Principles of Fluid Mechanics.* Allyn and Bacon, Inc., Boston, 1968.

[23] D.A. Anderson , J.C. Tannehill and R.H. Pletcher. *Computational Fluid Mechanics and Heat Transfer.* Series in Computational Methods in Mechanics and Thermal Sciences, Hemisphere, New York, 1984.

[24] D.C. Wilcox. *Turbulence Modelling for CFD.* DCW Industries, Inc., La Cañada, California, 1993.

[25] A. Berry. Flow Over a Backwards Facing Step. *University of Glasgow, Aerospace Engineering, Summer School in CFD*, September 1997.

[26] C.I.R.A. , Italian Aerospace Research Center. *First Europe-US High Speed Flow Field Database Workshop - Part II.* Naples, Italy. `http://www.cira.it/hsff-2/`, November 12-14, 1997.

[27] GARTEUR Action Group 24. Unpublished ONERA experimental data.

[28] GARTEUR Action Group 24. Unpublished ONERA computational results.

[29] X. Zheng, C. Liao, C. Liu, C.H. Sung and T.T. Huang. Multigrid Methods for Two-Equation Turbulent Models. *Lecture Notes for the Short Course "Advances in Computational Fluid Dynamics"*, Louisiana Tech University, Ruston, Louisiana, `http://www-math.cudenver.edu/~xzheng/publ.html`, June 24-28, 1996.

[30] F.R. Menter. Zonal Two Equation $k-\omega$ Turbulence Models for Aerodynamic Flows. *AIAA-93-2906*, 1993.

[31] A. Hellsten. Implementation of a One-Equation Turbulence Model into the FINFLO Flow Solver. *Helsinki University of Technology, Laboratory of Aerodynamics, Report No. B-49*, September 17, 1996.

[32] J. Henderson. Study of Slender Body Aerodynamics using PMB2D. *University of Glasgow, Aerospace Engineering Final Year Project*, April 1997.

[33] J. Delery and R.G. Lacau. Prediction of Base Flows. In *AGARD-FDP-VKI Special Course on Missile Aerodynamics*, April 3, 1987.

[34] GARTEUR Action Group 09. *Flow past Missile Afterbodies, Final Report.* GARTEUR TP no. 061, Main Part, 1991.

[35] J. Sahu and K.R. Heavey. Numerical Investigation of Supersonic Base Flow with Base Bleed. *Journal of Spacecraft and Rockets*, 34(1):62–69, 1997.

[36] B.J. Guidos. Navier-Stokes Computations of Finned Kinetic Energy Projectile Base Flow. *Journal of Spacecraft and Rockets*, 34(4):471–477, 1997.

[37] J. Sahu. Numerical Computations of Supersonic Base Flow with Special Emphasis on Turbulence Modelling. *AIAA Journal*, 32(7):1547–1549, 1994.

[38] GARTEUR Action Group 09. *Flow past Missile Afterbodies, Final Report.* GARTEUR TP no. 061, Appendix 3, 1991.

[39] C.G. Speziale. On Nonlinear $K-l$ and $K-\epsilon$ models of turbulence. *Journal of Fluid Mechanics*, 178:459–475, 1987.